

UNIVERSITÀ
DI PAVIA

Dipartimento di Fisica "A. Volta"

Corso di laurea magistrale in Scienze fisiche

Generation of Energy-Dependent Radiobiological Parameters for BNCT Using the BIANCA Biophysical Model

Tesi per la laurea di:

Camila Alejandra Costa Vargas

Supervisor:

Prof. Ricardo Luis Ramos

Co-Supervisors:

Prof. Francesca Ballarini

Prof. Ana Mailén Dattoli Viegas

Anno accademico 2025 – 2026

ABSTRACT

Boron Neutron Capture Therapy (BNCT) is a binary radiotherapy modality based on the selective accumulation of ^{10}B in tumor cells followed by low-energy neutron irradiation. The resulting nuclear reactions produce short-range, high-Linear Energy Transfer (LET) charged particles, creating a complex mixed radiation field whose biological effectiveness varies strongly with particle type, energy spectrum, and cellular radiosensitivity. Precise radiobiological characterization of these secondary radiation components is therefore crucial for accurate BNCT treatment planning and risk evaluation.

This thesis investigates the application of the BIANCA (Biophysical ANalysis of Cell death and chromosome Aberrations) biophysical model to generate cell-specific, energy-dependent radiobiological parameters (α and β) and evaluate their integration into the extended Photon Isoeffective Dose model. Radiobiological databases were extended or generated for four human cell lines: human skin fibroblasts (HSF), immortalized human keratinocytes (HaCaT), head and neck squamous cell carcinoma (HNSCC) and U-87 glioblastoma cells. Pre-existing databases were extended to high-LET regimes relevant to BNCT secondary particles, reaching up to 40 keV/μm for protons and 230 keV/μm for helium ions. A comprehensive database was generated for U-87 cells by calibrating baseline photon parameters against experimental ^{60}Co survival data and validating predictions against published ion-beam experimental datasets.

To overcome the breakdown of standard full-traversal track assumptions for low-energy particles, a novel effective-track model was developed for short-range protons whose physical ranges are comparable to or smaller than nuclear dimensions. The application of this formalism to HSF cells demonstrated the importance of explicitly accounting for the range of low-energy protons when predicting their radiobiological effectiveness.

Finally, the generated radiobiological databases were implemented into Photon Isoeffective Dose calculations within a phantom irradiation scenario utilizing an epithermal neutron beam. Two dosimetric methodologies were evaluated across superficial healthy tissue (1.1 mm depth) and a deeper thermal-peak tumor region (2.25 cm depth): an extended formulation explicitly binned by particle energy (D_{IsoE1}) and a reaction-weighted approximation (D_{IsoE2}). In superficial healthy tissue, the reaction-weighted approximation systematically overestimated the Photon Isoeffective Dose by approximately 5%, driven by the unmoderated recoil proton spectrum. In the tumor region, where thermal neutron capture reactions dominate, both models exhibited closer agreement, with the extended formulation predicting slightly higher effective doses.

Overall, this work demonstrates the capability of the BIANCA framework to deliver energy-dependent radiobiological input data across diverse cell lines and provides a robust methodological foundation for detailed, cell-specific biophysical dosimetry in BNCT.

ABSTRACT IN LINGUA ITALIANA

La Boron Neutron Capture Therapy (BNCT), o terapia per cattura neutronica del boro, è una modalità di radioterapia binaria basata sull'accumulo selettivo di ^{10}B nelle cellule tumorali, seguito dall'irradiazione con neutroni a bassa energia. Le reazioni nucleari risultanti producono particelle cariche ad alto trasferimento lineare di energia (LET) e con un range limitato nei tessuti, generando un campo di radiazione misto e complesso, la cui efficacia biologica dipende fortemente dal tipo di particella, dallo spettro energetico e dalla radiosensibilità cellulare. Una caratterizzazione radiobiologica accurata di queste componenti secondarie della radiazione è pertanto fondamentale per una corretta pianificazione dei trattamenti BNCT e per la valutazione dei rischi associati.

Questa tesi analizza l'applicazione del modello biofisico BIANCA (Biophysical ANalysis of Cell death and chromosome Aberrations) per generare parametri radiobiologici (α e β) specifici per ciascuna linea cellulare e dipendenti dall'energia, e per valutarne l'integrazione nel modello esteso di Photon Isoeffective Dose. Sono stati ampliati o sviluppati database radiobiologici per quattro linee cellulari umane: fibroblasti cutanei umani (HSF), cheratinociti umani immortalizzati (HaCaT), cellule di carcinoma squamocellulare della testa e del collo (HNSCC) e cellule di glioblastoma U-87. I database preesistenti sono stati estesi a regimi di LET elevato, rilevanti per le particelle secondarie prodotte nella BNCT, raggiungendo valori fino a 40 keV/μm per i protoni e 230 keV/μm per gli ioni elio. Inoltre, è stato sviluppato un database completo per le cellule U-87, calibrando i parametri di riferimento per i fotoni sulla base di dati sperimentali di sopravvivenza cellulare ottenuti con radiazione ^{60}Co e validando le previsioni mediante il confronto con dati sperimentali pubblicati relativi a fasci ionici.

Per superare i limiti delle ipotesi convenzionali del modello, che considerano traiettorie che attraversano completamente il nucleo cellulare, è stato sviluppato un nuovo modello di traccia efficace (effective-track model) per protoni a corto range, il cui percorso nel mezzo è confrontabile con le dimensioni del nucleo cellulare o inferiore a esse. L'applicazione di questo formalismo alle cellule HSF ha dimostrato l'importanza di considerare esplicitamente il range dei protoni a bassa energia nella previsione della loro efficacia radiobiologica.

Infine, i database radiobiologici generati sono stati implementati nei calcoli della Photon Isoeffective Dose nell'ambito di uno scenario di irradiazione di un fantoccio mediante un fascio di neutroni epitermici. Sono state valutate due metodologie dosimetriche, considerando un tessuto sano superficiale (a una profondità di 1.1 mm) e una regione tumorale più profonda, in corrispondenza del picco di neutroni termici

(a una profondità di 2.25 cm): una formulazione estesa con suddivisione esplicita delle particelle in intervalli energetici (D_{IsoE1}) e un'approssimazione pesata in base alle reazioni nucleari (D_{IsoE2}). Nel tessuto sano superficiale, l'approssimazione pesata in base alle reazioni ha sistematicamente sovrastimato la Photon Isoeffective Dose di circa il 5%, principalmente a causa dello spettro dei protoni di rinculo non ancora moderati. Nella regione tumorale, dove predominano le reazioni di cattura dei neutroni termici, i due modelli hanno mostrato una maggiore concordanza, con la formulazione estesa che ha previsto dosi efficaci leggermente superiori.

Nel complesso, questo lavoro dimostra la capacità del modello BIANCA di fornire parametri radiobiologici dipendenti dall'energia per diverse linee cellulari e offre una solida base metodologica per lo sviluppo di una dosimetria biofisica dettagliata e specifica per ciascun tipo cellulare nell'ambito della BNCT.

Contents

1 Introduction 7

1.1 Boron Neutron Capture Therapy 7

1.1.1 BNCT in clinic 8

1.2 Dosimetry in BNCT 9

1.2.1 Dose components of BNCT 9

1.2.2 RBE-weighted dose model 11

1.2.3 Photon Isoeffective dose model 12

1.2.3.1 Independent action 14

1.2.3.2 Synergistic action 16

1.2.4 Extension of the Photon Isoeffective dose model 17

2 Materials and Methods **19**

2.1 Generation of radiobiological parameters 19

2.1.1 The BIANCA biophysical model 19

2.1.2 Prediction of cell survival curves for an arbitrary cell line 21

2.1.3 Cell lines of interest 23

2.1.4 Extension of existing cell survival databases to the LET range relevant to BNCT 24

2.1.5 Full generation of a cell survival database 26

2.1.6 Development of an effective-track model for short-range protons in BIANCA 28

2.1.6.1 Application to human skin fibroblasts (HSF) 32

2.2 Application of the extended Photon Isoeffective dose model 34

2.2.1 Conceptual study in a simple geometry 34

2.2.2 Dose calculation approaches 35

3 Results and Discussion **37**

3.1 Cell-specific radiobiological parameters 37

3.1.1 Extension of pre-existing cell survival databases 37

3.1.2 Generation and validation of the U-87 radiobiological database 40
3.1.3 Short-range proton modeling in HSF cells 45
3.2 Evaluation of the photon isoeffective dose 48
3.2.1 Healthy tissue region 48
3.2.2 Tumor tissue region 52

4 Conclusions **56**

Appendix **59**

Bibliography **63**

List of figures **71**

List of Tables **72**

Acknowledgment **73**

Chapter 1

Introduction

1.1 Boron Neutron Capture Therapy

Boron Neutron Capture Therapy (BNCT) is a non-invasive form of binary radiotherapy that exploits the high cross section at thermal neutron energies (0.025 eV) of ^{10}B in boron-loaded tumor cells. The neutron capture reaction $^{10}B(n,\alpha)^{7}Li$ generates short-range high-linear energy transfer (LET) particles ($5-9\mu m$), which, in theory, selectively target tumor cells while leaving healthy tissue unharmed [1, 2].

The capture process forms an excited nucleus ($^{11}B^{*}$) that, due to its short half-life ($\tau \sim 10-12s$), decays almost immediately via two branches:

$$^{10}\mathrm{B} + \mathrm{n_{th}}\ (0.025\ \mathrm{eV}) \longrightarrow [^{11}\mathrm{B}^{*}] \begin{cases} \xrightarrow{6.3\%} {}^{4}\mathrm{He} + {}^{7}\mathrm{Li} \\ \xrightarrow{93.7\%} {}^{4}\mathrm{He} + {}^{7}\mathrm{Li} + \gamma\ (0.48\ \mathrm{MeV}) \end{cases} \tag{1.1}$$

In both branches of reaction, two highly ionizing particles are produced: alpha particles (^{4}He) and lithium-7 recoil nuclei (^{7}Li). For the dominant reaction branch, their initial kinetic energies are approximately 1.47 MeV and 0.84 MeV, respectively. Both particles have short ranges, comparable to cellular dimensions, and high LET values that vary along their trajectories as they lose energy in tissue. Consequently, they deposit their energy locally, potentially inducing severe DNA damage and cell inactivation.

The key aspects involved in therapy are:

- Administration of boron-enriched compounds capable of accumulating in the tumor.
- Low-energy neutron irradiation via a thermal or epithermal neutron beam.

Its success is determined by a sufficient amount of ^{10}B delivered selectively and the absorption of enough thermal neutrons to cause tumor cell inactivation.

An effective BNCT transport agent should have low toxicity, a boron-10 concentration of $\sim 20\mu g\,/\,g\,of\,tumor$, and be rapidly drained from healthy systems while remaining in the tumor throughout treatment [3]. However, of the only agents approved for clinical trials, BPA (boronophenyl alanine) and BSH (sodium borocaptate), neither of them fulfills the mentioned requirements to the fullest extent [1]. For example, one of the key aspects, boron accumulation, often does not reach optimal levels of clinical treatment. Where BSH is often insufficient, and even BPA is, despite their selectivity of absorption. In the third generation of boron agents the efforts are mainly directed toward the delivery of therapeutic amounts of boron with minimal levels of toxicity in normal cells and the tumor-targeting capability of these agents by the incorporation of tumor-targeting molecules, such as peptides, proteins, antibodies, nucleosides [4].

1.1.1 BNCT in clinic

Thermalized neutrons were the first type of neutrons used for clinical trials along with the compounds: sodium decahydrodecaborate ($Na_2B_{10}H_{10}$) for Brookhaven National Laboratory (BNL) in New York and BSH for the studies carried out in Japan by Hatanaka and Nakagawa as boron delivery agents [5, 6]. In both scenarios, head tumors were the primary target; however, only the Japan team was able to obtain promising results. This caused a pause in the clinical trials in the US that were resumed 30 years later but utilizing epithermal neutrons.

Gliomas, and in particular Glioblastoma Multiforme (GBM), are the most extensively studied tumors chosen in BNCT studies due to their highly invasive nature, lack of clear borders and the fact that they cannot be completely cured by surgery alone [7]. Although external radiation therapy is the widely used treatment in conjunction with surgery, its high probability of tumor regrowth, even at high LET, has led to the development of alternative therapeutic modalities, among which is BNCT. GBM is the most aggressive stage of gliomas, invading healthy brain tissue and traveling along nerve fibers and blood vessels far away from the primary tumor mass. Surgeons cannot eliminate these without causing severe neurological damage and standard radiation fields cannot target them safely. However, since BNCT relies on a chemical carrier to ideally flag only tumor cells at the microscopic level, it can selectively destroy those malignant cells. Today, the last phase of BNCT research has proven to be very promising by the work of Kawabata et al, who recently treated 22 patients with GBM in a phase II clinical trial in an irradiation facility in Japan [8].

As mentioned previously, another essential requirement for a successful BNCT is the sufficient emission of thermal neutrons (for shallow tumors) or epithermal neutrons (for deep-seated tumors) to be delivered to each boroneated tumor cell. The basic requirement for the production of suitable treatment neutron beams is an adequate epithermal fluence rate for therapy ($10^9 neutrons/cm^2 s$ at the therapy position) [6] while sufficiently suppressed fast neutron and gamma ray contamination to be acceptable. Historically, BNCT has been applied in institutions equipped with research nuclear reactors, which through the appropriate use of Beam Shaping Assemblies (BSA) were able to reach the desired fluxes mentioned above.

Today, Accelerator-Based Boron Neutron Capture Therapy (AB-BNCT) can produce a neutron flux of the same order through (p,n) or (d,n) reactions on beryllium or lithium targets. Due to their major advantages over reactor-based neutron sources, such as a less energetic neutron energy spectrum from certain nuclear reactions and the simplicity in installation and maintenance, they are considered the future modality of therapy. Cyclotrons and other accelerators, electrostatic or Radio Frequency Quadrupole (RFQ) projects for BNCT are already being developed and installed, with 26 AB-BNCT projects worldwide, 15 focused on clinical applications and 11 dedicated to research [9].

In Italy, the National Institute for Nuclear Physics (INFN) has developed a Radio Frequency Quadrupole (RFQ) proton accelerator capable of producing a 5 MeV, 30 mA proton beam. The beam impinges on a beryllium (Be) target, generating neutrons that are subsequently moderated and shaped by a Beam Shaping Assembly (BSA) to obtain a neutron flux of the order of 10^9 $cm^{-2}s^{-1}$, as required for clinical BNCT applications [10]. Within the framework of the ANTHEM project (PNC-PNRR), a new BNCT center is being developed in Caserta, including the installation of the INFN accelerator. The present thesis was carried out within the framework of this project, contributing to the radiobiological characterization of the secondary radiation field produced in BNCT.

1.2 Dosimetry in BNCT

1.2.1 Dose components of BNCT

For every radiotherapy technique, the precision with which the dose to be deposited in the tissues is calculated determines the safety and effectiveness of each treatment. In BNCT, the calculation of the total absorbed dose presents a particular challenge related to the nature of the interaction of radiation with biological matter. Scattering is the main way epithermal neutrons deposit energy in biological tissue, losing kinetic energy through multiple elastic collisions with a moderator (hydrogen in our case);

which results in what is known as neutron thermalization. Since neutrons do not react exclusively with boron but other highly abundant elements in matter, as shown in Figure 1.1, a mixed field of radiation is produced [11]. Each component of this field has a different biological effectiveness that must be addressed individually.

The most important capture reactions that produce significant energy deposition are $^{1}H(n,\gamma)^{2}H$ and $^{14}N(n,p)^{14}C$. However, these radiation components constitute a non-selective source of dose due to their broad-spectrum that affects both malignant and healthy cells alike. A highly localized energy released by targeted secondary particles is essential for the therapeutic dose. The selective dose component comes exclusively from the emitted particles of the reaction $^{10}B(n,\alpha)^{7}Li$ that even in the presence of low concentrations of boron constitutes most of the absorbed dose.

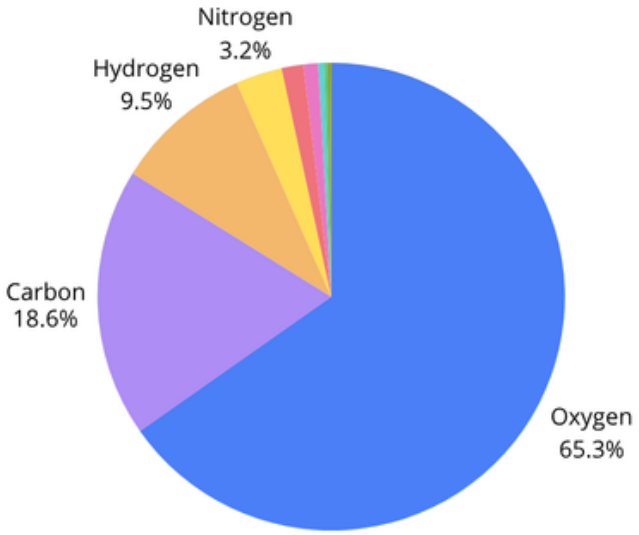


Figure 1.1: Most abundant elements found in the human body in percentage of total body weight [12]

The total absorbed dose (D) is the combination of the following four terms:

1. **Boron dose (D_1):** the most relevant component, as it is the therapeutic one, using the short range of the emitted particles (α and ^{7}Li) to localize the damage almost exclusively in the tumor.

2. **Fast neutron dose (D_2):** Epithermal/fast neutrons collide with the abundant ^{1}H nuclei in the tissue generating intermediate LET protons as a result of the reaction. The energy deposited by the recoil proton contributes to the overall dose delivered to the tissue, making it a significant component of the total dose.

3. **Thermal neutron dose (D_3):** thermalized neutrons interact with nitrogen via the reaction $^{14}N(n,p)^{14}C$ whose main product is a proton with an energy of approximately 0.58 MeV and LET in soft tissue of approximately 38 $keV/\mu m$. In this range, the particle is considered highly ionizing; therefore, added to the abundance of nitrogen, we cannot ignore this component of the absorbed dose.

4. **Total gamma dose (D_4):** different sources contribute to this dose, the capture reaction $^1H(n,\gamma)^2H$ being the one with the greatest contribution. The photon emitted has an energy of 2.2 MeV that allows it to go deep into the tissue, depositing energy far from their origin. This means that radiobiological effects may extend beyond the target area, potentially affecting healthy tissue. Other contributions are the intrinsic photon contamination of the neutron beam and the photon coming from the de-excitation of ^7Li.

The heterogeneous biological effect of the BNCT dose makes it necessary to convert to an equivalent reference dose, for which the dose-effect relationship is well defined. Given the extensive clinical and radiobiological knowledge produced over the years, the chosen reference radiation is photon radiation [13]. Therefore, the dose administered in BNCT will be translated into photon equivalent units (Gy (IsoE)) to predict the therapeutic effect and compare the results with other radiotherapy approaches. Once the dose is expressed in photon-equivalent units, it is possible to produce a treatment plan that maximizes the therapeutic effect while limiting the dose absorbed by normal tissues below the tolerance limits.

1.2.2 RBE-weighted dose model

The conventional model for the calculation of the equivalent dose of BNCT is the RBE-weighted dose model, which performs the conversion by weighting each dose component by its Relative Biological Effectiveness (RBE) or Compound Biological Effectiveness (CBE) [14]. Both factors represent the ratio between the absorbed dose due to reference photon radiation and the dose of the radiation studied that is needed to cause the same biological effect, with the difference that CBE refers to the dose component of boron.

$$D_{BNCT} = CBE_1 \cdot D_1 + RBE_2 \cdot D_2 + RBE_3 \cdot D_3 + RBE_4 \cdot D_4 \tag{1.2}$$

Both RBE and CBE are determined by radiobiological experiments for a given biological system calculated at fixed endpoints, for example, at 1% of cell survival in in-vitro experiments [13]. This means that the accepted factors are single numbers

derived from these different studies, assumed to be 'representative' of the relative effectiveness of each radiation component. However, this is not taking into consideration their dependency on the dose rate, leading to an overestimation of the photon equivalent dose and causing inconsistencies with the clinical effects reported in conventional radiotherapy.

1.2.3 Photon Isoeffective dose model

The consideration of fixed-RBE values represents a problem in terms of clinical applications since they are not sufficient to understand the observed clinical results of BNCT in terms of the photon radiotherapy data. A study carried out by Gonzalez et al [15] proposes a new formalism that takes advantage of all the experimental information available from cell survival experiments in order to accurately relate the observed effects to the corresponding end results in a standard photon radiation therapy.

The mentioned paper [15] presents a hypothetical case of brain tumors in which the RBE-weighted and photon-isoeffective doses were calculated and compared. In other words, it is a comparison between the dose calculations carried out in current BNCT clinical practice with those computed by means of the proposed general approach. The cell survival dose-response relationship is adequately described by the linear quadratic model (LQ), as described later, which accounts for dose-rate-dependent sublesion repair, hence referred to as the modified LQ model (MLQ). Figure 1.2 shows that the proposed approach yields isoeffective doses that are much lower than those of the fixed RBE method, although it does not consider additional actions, such as synergy.

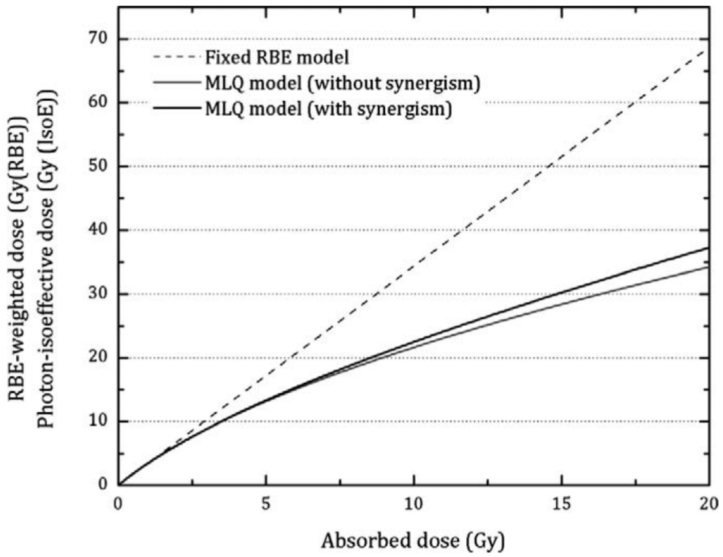


Figure 1.2: RBE-weighted dose (dashed line) and the photon-isoeffective doses calculated assuming independent action (solid gray line) or synergistic action (solid black line) as a function of the total absorbed dose [15].

Assuming that the RBE values are independent of each other leads to erroneous results, as shown above. For this reason, the development of a new formulation is proposed. The main principles considered are as follows:

- First-order repair of cellular sublethal lesions by means of a generalized factor, known as the Lea-Catcheside factor.
- Synergistic interactions between different radiations.

The core of the Theory of Dual Radiation Action (TDRA), in its initial and more advanced versions [16, 17], is that cellular lethal lesions arise from the direct action of single events or the random interaction of two independent events that together produce damage entities that produce a lethal lesion.

The trend that the average yield of lethal lesions follows in the first case is proportional to the absorbed dose. In the second case, to a rate proportional to the square of the dose. The correlation of the average yield per cell of these lesions with the survival fraction comes from assuming that one lesion is enough to inactivate a cell and that the number of lethal lesions is Poisson distributed, which leads to the description of cell survival according to the linear quadratic model (LQM)[18, 19]:

$$S(D) = e^{-(\alpha D + \beta D^2)}. \tag{1.3}$$

Here the coefficients α and β are related to the linear dependence where the lethality of the cell is proportional to the damage per single hit, and the quadratic dependence that links the lethality of the cell to the damage per sum of sublethal damages,

respectively. A lesion that cannot generate enough damage to cause cell death by itself is classified under the name of sub-lethal damage (SLD). The probability of producing a lethal lesion depends on the interaction between them, assuming their coexistence in space and time. Despite the fact that the main cause that leads to cell inactivation is a break in the double helix of DNA, this is not always the case. In general, if the cells are normal, the damage can be repaired very easily. However, in tumor cells the damage repair mechanisms are, in general, less effective.

First-order lesion repair was first studied in the groundbreaking work of Lea and Catcheside [18, 19], and was later generalized to include any dose delivery scheme [16, 20]. In the modified linear-quadratic formalism, the probability that a sublethal damage will not recombine with another sublethal damage because it has already been repaired is given by the generalized Lea-Catcheside time factor, G

$$G(\theta, t_0) = \frac{2t_0}{\theta}\left(1 - \frac{t_0}{\theta}\left(1 - e^{-\frac{\theta}{t_0}}\right)\right) \tag{1.4}$$

The G values are in a range between 0 and 1, where $G = 1$ means that all damage has combined with other damage and $G < 1$ that there is no recombination, so the cell has managed to repair the damage, which corresponds to greater cell survival. In the context of the linear-quadratic formalism, it modifies the quadratic term. Another important aspect is that this model does not take into account the distance between two sublethal damages, but only the temporal aspect, which corresponds to the irradiation time θ and the characteristic repair time t_0.

The simplest model considers that the cell has only one time to repair sublethal damage, as shown in equation 1.4. However, since not all sublesions have the same level of complexity, it is necessary to distinguish between two characteristic times to repair sublethal cell damage: a fast and a slow component. The expression to describe the G factor in function of the double kinetics of slow t_{os} and fast t_{of} repair goes as follows [21]:

$$G_k(\theta, t_{of}, t_{os}) = a_{kf} G(\theta, t_{of}) + a_{ks} G(\theta, t_{os}) \tag{1.5}$$

1.2.3.1 Independent action

According to the formalism presented in [15] the boron, thermal neutron, fast neutron and γ absorbed dose components of the BNCT mixed field are denoted $D_1, \ldots, D_4$ and the reference radiation R is named D_R. The aim is to find the photon isoeffective dose (previously referred to reference radiation) $D_R = D_R(D_1, D_2, D_3, D_4)$ that produces the same cell survival level as the combination of D_1, D_2, D_3, D_4.

The survival probability for the combination of the four dose components is $S(D_1, D_2, D_3, D_4)$.

If we consider the different radiations to be independent events, the overall probability of survival is the product of the probability of cell survival due to each radiation component

$$S(D_1,\ldots,D_4)=\prod_{i=1}^{4}S_i(D_i) \tag{1.6}$$

Let $S_R=S_R(D_R)$ be the probability for the reference photon radiation D_R. Therefore, the desired dose is the unique dose of the reference radiation that satisfies the equality:

$$S_R(D_R)=S(D_1,\ldots,D_4) \tag{1.7}$$

The next assumption is related to the cell survival of the *i-th* component, where only the dose components due to low-LET radiation can generate sublethal damage, and thus exhibit a quadratic dose dependence:

$$S_i(D_i)=\begin{cases} e^{-\alpha_i D_i} & i \quad =1,2,3 \\ \\ e^{-\alpha_i D_i+G_i(\theta)\beta_i D_i} & i \quad =4 \end{cases} \tag{1.8}$$

where α_i and β_i are the coefficients of the single-fraction linear-quadratic survival model for the corresponding radiations as well as the radiobiological parameters and $G(\theta)$ represents the generalized Lea-Catcheside factor for the γ component of the BNCT beam. Turning equation 1.7 into:

$$-ln(S_R(D_R))=\sum_{i=1}^{4}\alpha_i D_i+G_4(\theta)\beta_4 D_4^2 \tag{1.9}$$

Where

$$D_R(D_1,\ldots,D_4)=\sum_{i=1}^{4}r_i(D_R)D_i. \tag{1.10}$$

and

$$r_i(D_R)=\begin{cases} \alpha_i \frac{D_R}{(-ln(S_R(D_R))} & i \quad =1,2,3 \\ \\ (\alpha_i+G_i(\theta))\beta_i D_i \frac{D_R}{(-ln(S_R(D_R))} & i \quad =4 \end{cases} \tag{1.11}$$

The factors r_i represent the RBE coefficients as a function of the reference dose D_R. In the case of the gamma component ($i=4$), the repair of sublethal damage and the time course of dose deposition is taken into account through the generalized Lea-Catcheside factor.

Similarly, we take the reference dose and assume that its survival is given by the single-fraction linear-quadratic dose expression:

$$-ln(S_R(D_R)) = \alpha_R D_R + G_R(\theta')\beta_R D_R^2 \tag{1.12}$$

where α_R and β_R are the coefficients of the linear-quadratic model, while $G_R(\theta')$ represents the generalized Lea-Catcheside time factor for the reference radiation. This expression is used to rewrite equation 1.10 as:

$$D_R(D_1,\ldots,D_4) = \sum_{i=1}^{3}\left(\frac{\alpha_i}{\alpha_R + G_R(\theta')\beta_R D_R}\right)D_i + \left(\frac{\alpha_4 + G_4(\theta)\beta_4 D_4}{\alpha_R + G_R(\theta')\beta_R D_R}\right)D_4 \tag{1.13}$$

This expression can be considered an appropriate expression to calculate the photon-isoeffective dose in the mixed-LET BNCT radiation field since the given RBE/CBE factors, corresponding to the factors in brackets multiplying D_i, depend on the dose D_R, which implies that they are not fixed values. Additionally, in order to obtain D_R it must be solved numerically.

However, an analytical expression of D_R can be obtained under the following considerations:

- If cell survival experiments are carried out with a constant irradiation time, which means that $G_R(\theta') = G_R$ is constant.
- If variations of $G_R(\theta')$ during irradiation can be neglected, G_R is approximately constant. This can occur, for example, in the case where the irradiation time is shorter than the characteristic repair time.

Equation 1.13 becomes:

$$D_R(D_1,\ldots,D_4) = \frac{1}{2}\cdot\frac{(\alpha/\beta)_R}{G_R}\cdot\left(\sqrt{1 + \frac{4G_R}{\alpha_R(\alpha/\beta)_R}\left(\sum_{i=3}^{3}\alpha_i D_i + G_4(\theta)\beta_4 D_4^2\right)} - 1\right) \tag{1.14}$$

In this expression, the RBE factors do not appear explicitly; rather, there is a direct dependence on the radiobiological parameters α and β of the LQ model, both for the BNCT field and for the reference radiation.

1.2.3.2 Synergistic action

Sublethal lesions produced by different radiations that coexist in space and time have a finite probability of interacting and producing an additional effect that cannot be defined by the simple sum of the two radiations. This effect is known as radiation

synergism and introduces mixed terms into the LQ formalism, which are modulated by appropriate Lea-Catcheside factors [22].

To include synergism in the model, we consider that sublethal lesions from different radiations combine to produce lethal damage. For each component i the yield of sublethal damage per unit dose is given by $\sqrt{\beta_i}$. The cell survival for the radiation type is then expressed by:

$$-ln(S_i(D_i)) = \alpha_i D_i + G_i(\theta)\beta_i D_i^2 \tag{1.15}$$

The synergism between two components i and j, derived from the TDRA model, can be described by the expression:

$$-ln(S_i(D_i, D_j)) = G_{ij}(\theta)\sqrt{\beta_i\beta_j}D_i D_j \qquad i \neq j = 1,2,3,4 \tag{1.16}$$

where $G_{ij}(\theta)$ denotes the time factor that takes into account the first-order repair of the sublesions produced by radiation i $(or\ j)$ that reduces the probability of interaction with sublesions produced by radiation j $(or\ i)$ during irradiation. Then, the survival probability for the combination of the four radiations is:

$$-ln(S(D_1, D_2, D_3, D_4)) = \sum_{i=1}^{4}\alpha_i D_i + \sum_{i=1}^{4}\sum_{j=1}^{4} G_{ij}(\theta)\sqrt{\beta_i\beta_j}D_i D_j \tag{1.17}$$

This includes the quadratic term of Equation 1.16

Therefore, replacing the expressions 1.12 and 1.17 into Eq. 1.7 and solving the equation for D_R, the general photon isoeffective dose for BNCT is obtained

$$D_R(D_1,\ldots,D_4) = \frac{1}{2}\cdot\frac{(\alpha/\beta)_R}{G_R}\cdot\left(\sqrt{1+\frac{4G_R}{\alpha_R(\alpha/\beta)_R}\left(\sum_{i=4}^{4}\alpha_i D_i + G_{ij}(\theta)\sqrt{\beta_i\beta_j}D_i D_j\right)}-1\right) \tag{1.18}$$

1.2.4 Extension of the Photon Isoeffective dose model

The overall biological effect of the various radiation components in BNCT depends not only on the absorbed dose but also on the type and energy of the secondary charged particles involved. The extension of the photon isoeffective dose model evaluates the relevance of incorporating the energy dependence of secondary charged particles into BNCT dosimetry and to assess the impact on dose calculations. In the article presented by Dattoli et al [23] the original formalism, expressed in terms of BNCT dose components, is reformulated in terms of secondary charged particle fields resolved by

particle type and energy as:

$$D_R(D_1,\ldots,D_4) = \frac{1}{2}\cdot\frac{(\alpha/\beta)_R}{G_R}\left(\sqrt{1+\frac{4G_R}{\alpha_R(\alpha/\beta)_R}\left(\sum_{i=1}^{5}\sum_{k=1}^{N_i}\alpha_i(E_{ik})D_{ik} + \sum_{i,j=1}^{5}\sum_{k=1}^{N_i}\sum_{l=1}^{N_j}G_{ij}(\theta)\sqrt{\beta_i(E_{ik})\beta_j(E_{jl})}D_{ik}D_{jl}\right)}-1\right) \tag{1.19}$$

In this case, index i (or j) represents the particle type rather than the BNCT dose component. For each particle type i, N_i denotes the number of energy bins, E_{ik} represents the k-th energy (with $1 \leq k \leq N_i$), $D_{i,k}$ is the dose imparted by particles with energy E_{ik} , $\alpha_i(E_{ik})$ and $\beta_i(E_{ik})$ are the alpha and beta coefficients for particle type i at energy E_{ik} and G_{ij} is the Lea-Catcheside time factor.

This reformulation enables the explicit incorporation of radiobiological parameters that depend on both particle type and energy (or LET). The BNCT mixed radiation field includes several secondary charged particles, such as protons (^{1}H), alpha particles (^{4}He), lithium ions (^{7}Li), and carbon recoil nuclei (^{14}C), as well as electrons.

The application of the extended Photon Isoeffective Dose model requires the radiobiological parameters α and β to be characterized as functions of energy for each secondary particle type contributing to the BNCT radiation field. In this thesis, the BIANCA model is used to investigate these energy-dependent parameters, enabling the application of the extended formulation and its comparison with the reaction-based approach. The methodology adopted is described in the following section.

Chapter 2

Materials and Methods

2.1 Generation of radiobiological parameters

The aim of this section is to describe the generation of energy-dependent radiobiological parameters required for the application of the extended Photon Isoeffective Dose model to BNCT. Three complementary approaches were adopted. First, pre-existing BIANCA radiobiological databases for human skin fibroblasts (HSF), immortalized human keratinocytes (HaCaT), and head and neck squamous cell carcinoma (HNSCC) cells were extended to cover the LET ranges relevant to BNCT secondary charged particles. Second, a new radiobiological database was generated for U-87 glioblastoma cells. Third, the standard BIANCA treatment of proton tracks was revised to account for low-energy protons whose ranges become comparable to, or shorter than, the dimensions of the cell nucleus. To address this limitation, an effective-track model for short-range protons was developed and applied to HSF cells.

2.1.1 The BIANCA biophysical model

BIANCA stands for BIophysical ANalysis of Cell death and chromosome Aberrations, which is a biophysical model of radiation-induced cell death, implemented as a Monte Carlo code [24]. The idea behind BIANCA consists of capturing the concept that some of the various types of DNA damage induced by ionizing radiation are 'critical' for the cell fate, since cell death is the most probable outcome in the case of incorrect rejoining or unrejoining of the produced chromosomal fragments.

The main feature of the model consists of assuming that cell inactivation is due to certain types of chromosome aberrations and that chromosome aberrations derive from DNA cluster damage. More specifically, the following assumptions were adopted:

1. Radiation induces critical DNA lesions (CL), and by definition, each of them

produces two independent chromosome free-ends;

2. Only free-ends having initial distance below a threshold d participate in the end-joining process, which can lead to aberrations of the chromosomes in case of incorrect rejoining or "mis-rejoining". Although in the newest version of the model, a fragment un-rejoining probability has been introduced to take into account that not all fragments will undergo end-joining;

3. Major structural chromosome aberrations (dicentrics, rings, and large deletions) lead to clonogenic inactivation.

Assumptions (1) and (2) arise from the evidence that, on average, 1 Gy of radiation induces a double-strand break (DSB) yield on the order of $(30-40)$ DSB per cell, but only $1-2$ chromosome aberrations per cell or even less (depending on LET). A good candidate for the description of the complexity of severe damage is, in principle, a cluster of DSB. However, since the characterization of such critical lesions is still an open question [25], in the work of Carante *et al* [26] it is purposely decided not to give an a priori definition of "critical lesions" and consider the CL yield as the first parameter of the model. The value of this metric greatly depends on the radiation quality, but is also determined by the characteristics of the cell target including cell radiosensitivity, nucleus shape, and dimensions. In addition, it has an important influence on the absolute value of the cell surviving fraction at various doses.

In terms of simulation of cell survival, figure 2.1 captures the basic idea underlying the BIANCA approach, which is that some types of DNA damage (CLs) lead to chromosome aberrations through distance-dependent mis-rejoining, or un-rejoining, of chromosome fragments, and that some chromosome aberrations lead to clonogenic cell death [27]. The probability of end-joining of the chromosome fragment, P, is assumed to follow a step function whose value is determined by whether the distance d between two chromosome free-ends is smaller than a cut-off value d_0. Although in previous versions of the model [24, 28, 29] this cut-off distance was considered an adjustable parameter, in the latest it has been set to the mean distance between two adjacent chromosome territories [30]. Moreover, the fragment un-rejoining probability, f, is introduced in order to take into account that not all fragments are eventually rejoined with a partner even if they are between the threshold distance, being f the second and last parameter. Its values have been assumed to depend on the cell line and radiation quality, since in the most recent version it was found that the experimental cell survival curves considered were better reproduced by allowing f to increase with LET. Therefore, f influences the shape of the survival curve.

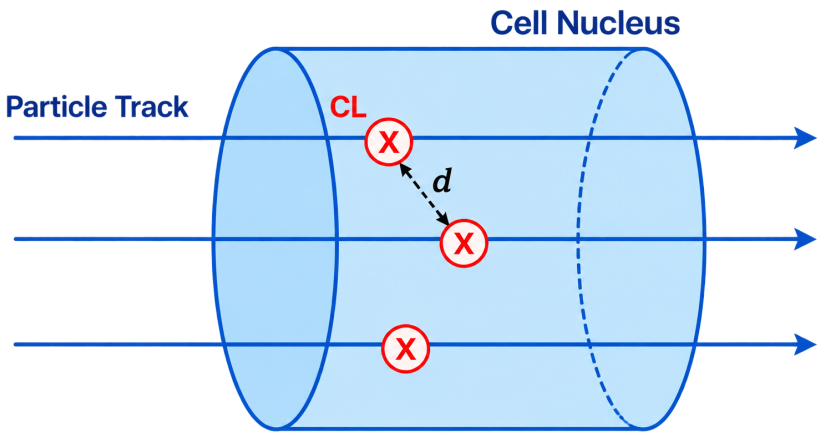


Figure 2.1: probability of end-joining of the chromosome fragments in terms of the distance between the free-ends d and a threshold value d_0, fixed as mean distance between two adjacent chromosome territories. If $d < d_0$ chromosomes can rejoin, with an un-rejoining probability. Otherwise, no rejoining occurs [27]

.

2.1.2 Prediction of cell survival curves for an arbitrary cell line

As described in the works [31, 32, 27] to perform a simulation with BIANCA the following input data are required

1. Radiation type, that is, photons, light ions (protons and He-ions) or heavy ions (C-ions);

2. The described model parameters, which are the CL yield and f values;

3. Shape and size of the cell nucleus, which currently can be modeled either by a sphere or by a cylinder, the latter with circular or elliptical base;

4. Physical characteristics of irradiation. For photons that is the absorbed dose and in the case of ion irradiation it also encompasses the LET of the particle and its energy.

The actual number of CLs induced in the nucleus depends on the irradiation type. For cells exposed to photons these CLs are uniformly distributed within the cell nucleus, while to light ions they are along (parallel) straight lines that represent the trajectory of the primary particle [27]. To make comparisons between cell types that have a different nucleus thickness, it is more practical to express the CL yield as the mean number of CLs per unit of traversal length. Here, the quantity will be expressed as a function of the dimensions of the nucleus.

In contrast, for heavier ions, each CL induced by a given ion is assumed to have a 0.5 probability of being induced along the primary-ion trajectory, and a 0.5 probability of being shifted radially, to model the effects of high-energy secondary electrons [27]. This equiprobability comes from the phenomena that take place in the track core and in the penumbra [33]. However, it does not affect the simulation outcomes, because the relevant information is whether a given CL falls in a certain chromosome territory or in another one, which is a micrometre-scale question.

According to previous works by Carante *et al* [27, 34, 35], cell survival curves of an arbitrary cell line after irradiation can be predicted starting from a known photon response of a reference cell line. V79 cells are the preferred choice for working as a reference due to their wide use in radiobiology. In particular, in the BIANCA model, it is chosen because the cell pathway that follows cell death is derived mainly from chromosome aberrations rather than from apoptosis and necrosis [32].

Survival data have been collected from the literature for protons [36, 37], ^{12}C ions [38] and ^{3}He ions [38] in certain LET ranges in order to reproduce, with the use of BIANCA, experimental survival curves in a dose range of up to 3 Gy by fitting the two model parameters mentioned before. This means that a CL yield and a f value have been associated with any LET, allowing us to simulate cell survival curves for many LET values. In turn, each of these curves has been fitted by the function of the linear-quadratic model:

$$S(D) = e^{(-\alpha D - \beta D^2)}. \tag{2.1}$$

This has allowed the construction of a table describing V79 cell survival consisting of pairs of radiobiological coefficients (α and β) for different ion types and LET values for ions with Z up to 8, as well as the two photon coefficients. More details can be found in [31, 27].

In principle, the CL yield for a given radiation quality should be adjusted separately for each cell line considered, since this parameter also depends on the radiosensitivity of the target cell. However, as detailed in [27, 34], the mean number of CLs per μm to predict the survival of an arbitrary cell line in a given LET can be derived by multiplying the value of the CL fitting function of V79 cells in that LET by the following factor:

$$\frac{CL}{\mu m} = \left(\frac{CL}{\mu m}\right)_{ref} \cdot \left[\left(\frac{CL}{Gycell}\right)_{X} \Big/ \left(\frac{CL}{Gycell}\right)_{X,ref}\right] \cdot \frac{V_{ref}}{V} \tag{2.2}$$

where $(CL/\mu m)_{ref}$ is the CL yield used for the reference cell line irradiated with the same radiation quality, while $(CL \cdot Gy^{-1} \cdot cell^{-1})_X$ and $(CL \cdot Gy^{-1} \cdot cell^{-1})_{X,ref}$ are the CL yields used to simulate photon irradiation of the cell line of interest and

the reference cell line, respectively, in terms of unit dose per cell. Finally, V_{ref} and V represent the nucleus volume of the reference cell line and the cell line of interest, respectively. The value of f is derived as follows:

$$f = f_{ref} + f_X + f_{X,ref} \tag{2.3}$$

In this equation, f_{ref} is the f value used for the V79 reference cell line exposed to the same radiation quality, whereas f_X and $f_{X,ref}$ are the f values used to simulate the photon survival curve of the cell line of interest and the reference cell line, respectively.

By this means, knowing the photon response of an arbitrary cell line of interest, equations 2.2 and 2.3 provide the CL yields and the f value to predict cell survival curves after irradiation of that cell line with different ion types over a wide LET or energy range. Each of these curves can then be fitted using equation 2.1, to obtain the desired radiobiological coefficients that will constitute the simulation database for each cell line of interest.

2.1.3 Cell lines of interest

Skin is an important dose-limiting organ in radiotherapy and also serves as a relevant model for investigating healthy tissue responses to radiation. For this reason, human skin fibroblasts (HSF) and immortalized human keratinocytes (HaCaT) are widely used in radiobiological studies and simulations [39].

The spontaneously immortalized HaCaT cell line was derived from adult human epidermal keratinocytes and retains the ability to proliferate and undergo differentiation. These characteristics make HaCaT cells a useful model for investigating the epidermal epithelial barrier and its response to radiation. In particular, their stable growth characteristics and non-tumorigenic nature make them suitable for reproducible in vitro studies [40].

Human skin fibroblasts (HSF) are cells of dermal origin that play an important role in maintaining the structural integrity of connective tissue, synthesizing extracellular matrix components such as collagen, and participating in tissue repair. In this work, the term HSF is used collectively to refer to normal human skin fibroblast cell lines represented in the experimental radiobiological data, rather than to a single specific cell line. Among these, AG01522 is a well-characterized human diploid fibroblast cell line derived from neonatal foreskin and widely employed in radiobiological investigations. Its extensive experimental characterization makes it particularly useful for studying radiation-induced biological effects in normal human cells [39, 41].

The main distinction between these healthy cell models lies in the tissues and cell

types they represent. HSF provide a model of dermal connective tissue, whereas HaCaT cells represent the epidermal keratinocyte component of the skin. Together, they allow the investigation of radiation responses in different skin cell populations and provide relevant reference data for evaluating biological effects in healthy tissues [40, 42].

As mentioned previously, head and neck squamous cell carcinoma (HNSCC) and U-87 glioblastoma cells are used as tumour models in this work. Glioblastoma is one of the most aggressive primary brain tumours in adults, characterized by infiltrative growth, resistance to conventional treatments, and a high recurrence rate following radiotherapy [43]. These characteristics make glioblastoma an important target for investigating alternative radiotherapeutic approaches, including particle therapy and BNCT. Head and neck squamous cell carcinomas are also relevant in the context of particle therapy, where the potential advantages of high-LET radiation have been investigated [44].

2.1.4 Extension of existing cell survival databases to the LET range relevant to BNCT

The pre-existing cell survival databases for human skin fibroblasts (HSF) [23], head and neck squamous cell carcinoma (HNSCC) [44], and immortalized human keratinocytes (HaCaT) [45] were restricted to maximum LET values of 30 keV/μm for protons and 190 keV/μm for helium ions ($^4He^{2+}$). However, in BNCT, neutron interactions produce secondary charged particles that can reach significantly higher LET values.

Specifically, the thermal neutron capture reaction $^{14}N(n,p)^{14}C$ (reaction 1 in Figure 2.2) produces protons with a characteristic initial kinetic energy of approximately 583 keV, corresponding to an initial LET in tissue of approximately 38 keV/μm. This value motivates the extension of the proton database up to 40 keV/μm. Elastic scattering on hydrogen, $^1H(n,n)p$ (reaction 2 in Figure 2.2), generates recoil protons spanning a broad energy spectrum, from low energies up to the energies of the incident fast neutrons ($\sim$ 2 MeV). Finally, the $^{10}B(n,\alpha)^7Li$ capture reaction (reaction 3 in Figure 2.2) produces alpha particles ($^4He^{2+}$) and ^7Li recoil nuclei with initial kinetic energies of approximately 1.47 MeV and 0.84 MeV, respectively, for the dominant reaction branch. The alpha particles have an initial LET in tissue of approximately 200–220 keV/μm, motivating the extension of the helium-ion database up to 230 keV/μm.

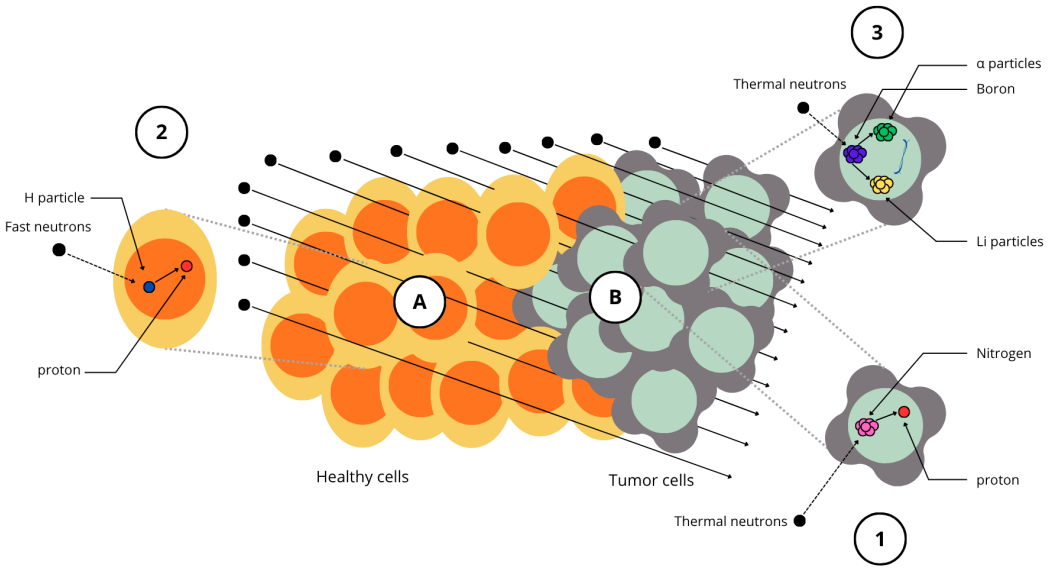


Figure 2.2: schematic representation of three nuclear reactions relevant to BNCT in healthy tissue (region A) and tumor tissue (region B). These reactions may occur in both regions, although their relative contributions depend on the local neutron energy spectrum, tissue composition, and boron concentration: (1) thermal neutron capture on nitrogen $^{14}\mathrm{N}(n,p)^{14}\mathrm{C}$, (2) neutron elastic scattering on hydrogen $^{1}\mathrm{H}(n,n)p$, and (3) thermal neutron capture on boron $^{10}\mathrm{B}(n,\alpha)^{7}\mathrm{Li}$.

As illustrated in Figure 2.2, the three reactions considered in this schematic can occur in both healthy and tumor tissues. However, their relative contributions depend on the local neutron energy spectrum, tissue composition, and boron concentration. In superficial healthy tissues (region A), the incoming beam contains a fast neutron component that interacts with hydrogen nuclei, contributing to neutron thermalization. Consequently, elastic scattering (reaction 2) can contribute significantly to the absorbed dose in superficial healthy tissues. To accurately evaluate the radiobiological impact of low-energy recoil protons, a short-range particle track model is introduced in Section 2.1.6, with specific application to HSF cells as a model of healthy skin tissue. In deeper regions (region B), neutron thermalization can favor capture reactions on $^{14}\mathrm{N}$ and $^{10}\mathrm{B}$ (reactions 1 and 3). The contribution of the boron capture reaction is particularly important in tumor regions where $^{10}\mathrm{B}$ preferentially accumulates.

Consequently, the upper boundaries of the original databases do not cover the full LET range relevant to BNCT secondary charged particles. Without extending these databases, the Photon Isoeffective Dose model must rely on mathematical extrapolations in high-LET regimes, introducing potential inaccuracies in the estimation of radiobiological parameters.

To overcome these limitations, the cell survival databases for HSF, HNSCC, and

HaCaT were extended to higher LET values for light ions ($Z \leq 4$). The proton database was extended to include LET values of 32.5, 35.0, 37.5, and 40.0 keV/μm, while the helium-ion database was extended to 200, 210, 220, and 230 keV/μm. Additionally, the short-range model developed in Section 2.1.6 was applied to HSF cells to construct an energy-based database spanning kinetic energies from 1 keV to 200 MeV.

Following the parameterization methodology outlined in Section 2.1.2, and once the photon response of the cell line is known, the procedure described by Equations 2.2 and 2.3 was employed to calculate the corresponding CL yield and fragment unrejoining probability (f) for helium ions using the parameters described in Tables 1 and 2. Using BIANCA simulations, cell survival curves were generated as a function of absorbed dose (up to 3 Gy). The resulting survival fractions were subsequently fitted with the linear-quadratic (LQ) model to obtain the α and β parameters required to complete the high-LET radiobiological databases for HNSCC and HaCaT. For HSF cells, the short-range track behavior of low-energy protons was additionally taken into account through the development of a dedicated effective-track model. The detailed procedure for this implementation is described in Section 2.1.6.

It is worth noting that the LET range for carbon ions was not extended, since the pre-existing database already covers the range considered relevant to BNCT in this work. Nevertheless, the final radiobiological databases for all cell lines of interest incorporate parameters for carbon ions. Within the BIANCA framework, carbon ions are modeled according to their atomic number ($Z = 6$), without isotope-specific distinctions. At a given velocity, the microscopic track structure of carbon ions is primarily governed by their nuclear charge, so the isotope dependence is neglected in this approximation [46]. Therefore, the label ^{14}C used throughout this work refers to carbon ions ($Z = 6$) produced in the $^{14}\mathrm{N}(n,p)^{14}\mathrm{C}$ reaction, whose radiobiological parameters are approximated using the $Z = 6$ dataset implemented in BIANCA and calibrated against experimental data obtained with ^{12}C ions.

2.1.5 Full generation of a cell survival database

As mentioned previously, the human glioblastoma cell line U-87 (also referred to as U-87 MG) was selected because it represents a widely used reference model for *in vitro* studies of human glioblastoma.

To construct a comprehensive radiobiological database within the BIANCA framework, the initial step requires establishing the baseline cell survival response following reference photon irradiation as a function of absorbed dose. Marcaccio et al. [47] demonstrated the importance of selecting a reference radiation quality that closely reflects clinical treatment conditions. In BNCT, one component of the mixed radia-

tion field consists of photon radiation, including 2.2 MeV γ-rays generated by thermal neutron capture on hydrogen (^{1}H$(n,\gamma)^2$H). Consequently, a reference photon quality closer in energy to this 2.2 MeV component is preferable. Between the two reference photon qualities evaluated in their work (X-rays and ^{60}Co γ-rays), ^{60}Co γ-rays were selected as the reference radiation for subsequent calculations and simulations.

The reported linear-quadratic radiobiological parameters for ^{60}Co photon irradiation ($\alpha = 0.21$ Gy^{-1} and $\beta = 0.02$ Gy^{-2}) were used to calibrate the photon-specific BIANCA parameters, namely the critical lesion (CL) yield and the fragment un-rejoining probability (f), required to predict U-87 cell survival following irradiation with different ion species (p, ^{4}He^{2+}, and carbon ions with $Z = 6$) over a range of LET values. The corresponding BIANCA parameters (CL and f) were calculated using the iterative calibration procedure detailed in Section 2.1.2.

To evaluate the predictive accuracy of the model, the simulation results were compared with published experimental cell survival datasets for glioblastoma cells exposed to photon, proton, and carbon-ion beams:

- **Chiblak et al. [48]:** U-87 cell cultures were irradiated with 320 kVp X-rays at doses of 0, 1, 2, and 4 Gy. Particle irradiations with protons at a LET of 2.5 keV/μm and carbon ions at a LET of 40 keV/μm were performed at the Heidelberg Ion-Beam Therapy Center (HIT), using a pencil beam to deliver a 1.5 cm spread-out Bragg peak (SOBP) centered at a water-equivalent depth of 14.0 cm.

- **Combs et al. [49]:** U-87 cells expressing wild-type p53 were irradiated with carbon-ion beams using either a monoenergetic beam (LET = 172 keV/μm) or an extended SOBP (LET = 103 keV/μm). The selection of experimental data from monoenergetic beams versus modulated SOBPs affects the physical complexity of the radiation field. Because biophysical parameterizations aim to establish a relationship between ion species, LET, and biological response, only experimental datasets obtained under monoenergetic irradiation conditions were considered for validation.

- **Chaudhary et al. [50]:** human glioblastoma U-87 cells were irradiated at six distinct depth positions along pristine and modulated 62 MeV proton beam profiles. The corresponding physical depths, dose-averaged LET values, and linear-quadratic parameters for positions P1 through P6 along the pristine 62 MeV proton beam are summarized in Table 3.

The resulting cell survival curves and their comparison with the experimental datasets described above are presented and discussed in the next chapter.

2.1.6 Development of an effective-track model for short-range protons in BIANCA

In BNCT, low-energy secondary protons are generated with kinetic energies ranging from a few keV to hundreds of keV. These particles can have physical ranges (R) comparable to or smaller than the characteristic nuclear traversal length (L_{cell}). Such protons can originate from elastic scattering of neutrons on hydrogen nuclei, as well as from the $^{14}\text{N}(n,p)^{14}\text{C}$ reaction. In particular, recoil protons produced by neutron scattering can contribute to the absorbed dose in healthy tissues exposed to the incoming neutron beam. Therefore, an accurate assessment of their biological effects is important for evaluating normal tissue complications.

In the standard implementation of the BIANCA biophysical model, charged particles are assumed to traverse the cell nucleus along a characteristic track length L_{cell}, with critical lesions distributed along this trajectory. Although this approximation is appropriate for particles whose ranges are much larger than nuclear dimensions, it becomes inadequate for low-energy protons that may stop within the cell nucleus [30]. Although conventional radiation transport tools can describe the energy deposition of short-range particles, their biological effects are not explicitly accounted for in the standard BIANCA implementation when predicting cell survival curves and the corresponding radiobiological parameters α and β. To overcome this limitation, an effective-track formalism was developed to incorporate short-range protons into the standard BIANCA simulation framework, providing a novel approach to predict the biological effectiveness of this dose component. The two proton transport regimes are schematically illustrated in Figure 2.3.

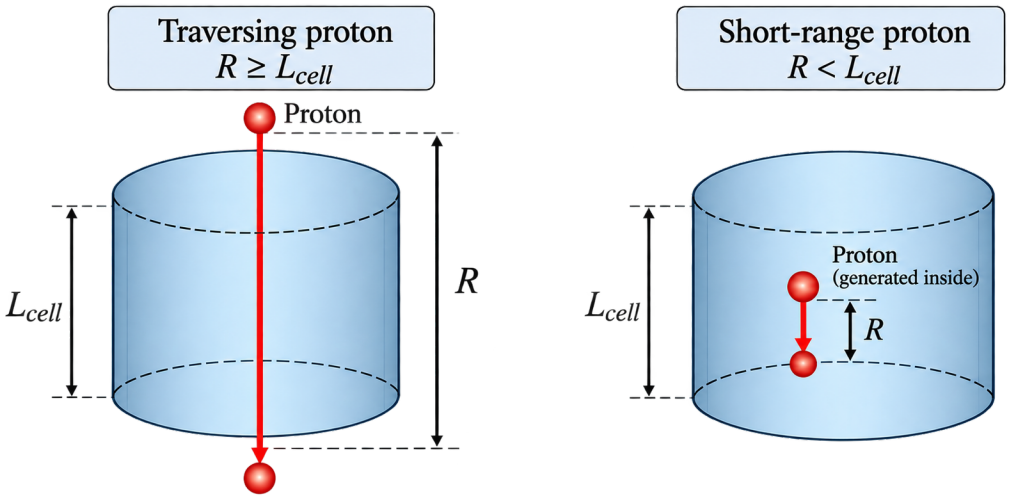


Figure 2.3: schematic representation of the two proton transport regimes considered in the effective-track formalism. (a) Traversing proton, with a physical range $R \geq L_{\text{cell}}$, crossing the cell nucleus along its characteristic traversal length L_{cell}. (b) Short-range proton, with $R < L_{\text{cell}}$, stopping within the cell nucleus.

The particle transport regime is determined by comparing the proton range R with the characteristic nuclear traversal length L_{cell}. Two limiting regimes and an intermediate transition region are considered.

Short-range regime

When $R < L_{\text{cell}}$, a proton stopping within the cell nucleus is considered. Its track-averaged linear energy transfer is defined as:

$$\text{LET}_{\text{track}} = \frac{E}{R} \tag{2.4}$$

where E is the initial kinetic energy of the proton, R is its physical range in the considered medium, and $\text{LET}_{\text{track}}$ represents the average energy deposited per unit length along the proton track, assuming that its entire kinetic energy is deposited over the distance R.

In standard BIANCA simulations, the absorbed dose D delivered to a cell mass m is calculated assuming full-length particle traversal (L_{cell}):

$$D = \frac{\text{LET} \cdot L_{\text{cell}} \cdot N_{\text{BIANCA}}}{m} \tag{2.5}$$

where D is the absorbed dose, LET is the linear energy transfer assigned to each simulated particle, L_{cell} is the characteristic nuclear traversal length, N_{BIANCA} is the number of simulated particles required to deliver the prescribed dose, and m is the mass of the considered cell volume. This expression assumes that each simulated particle deposits

an energy equal to $\mathrm{LET} \cdot L_{\mathrm{cell}}$.

Directly using $\mathrm{LET}_{\mathrm{track}}$ as the BIANCA input would cause each simulated particle to deposit an energy $\mathrm{LET}_{\mathrm{track}} L_{\mathrm{cell}}$, rather than its actual kinetic energy E. Consequently, the number of simulated particles would be underestimated by a factor R/L_{cell} relative to the number required when each proton deposits its entire kinetic energy within the considered volume:

$$N_{\mathrm{real}} = \frac{D \cdot m}{E} \tag{2.6}$$

where N_{real} is the number of physical protons required to deliver the absorbed dose D, m is the mass of the considered volume, and E is the energy deposited by each proton, assumed equal to its initial kinetic energy.

To restore consistency, an effective input LET is defined as:

$$\mathrm{LET}_{\mathrm{BIANCA}} = \mathrm{LET}_{\mathrm{track}} \cdot \frac{R}{L_{\mathrm{cell}}} = \frac{E}{L_{\mathrm{cell}}} \tag{2.7}$$

where $\mathrm{LET}_{\mathrm{BIANCA}}$ is the effective LET assigned to each simulated particle, $\mathrm{LET}_{\mathrm{track}}$ is the track-averaged LET, and R/L_{cell} is the geometrical scaling factor accounting for the difference between the physical proton range and the characteristic traversal length used in BIANCA. This definition ensures that the energy deposited by each simulated particle, $\mathrm{LET}_{\mathrm{BIANCA}} L_{\mathrm{cell}}$, equals the initial kinetic energy E of the proton.

Consequently, the number of simulated particles becomes:

$$N_{\mathrm{BIANCA}} = \frac{D \cdot m}{\mathrm{LET}_{\mathrm{BIANCA}} \cdot L_{\mathrm{cell}}} = N_{\mathrm{real}} \tag{2.8}$$

where N_{BIANCA} is the number of simulated particles and N_{real} is the corresponding number of physical protons. Their equality follows from the definition of $\mathrm{LET}_{\mathrm{BIANCA}}$, ensuring consistency between the prescribed absorbed dose and the energy assigned to each particle in the short-range regime.

To maintain consistency in the predicted biological damage, the critical lesion yield CL, expressed as the mean number of critical lesions per unit track length, must also be rescaled. The mean number of critical lesions produced per proton is:

$$N_{\mathrm{CL}}^{\mathrm{real}} = CL\left(\mathrm{LET}_{\mathrm{track}}\right) \cdot R \tag{2.9}$$

where $N_{\mathrm{CL}}^{\mathrm{real}}$ is the mean number of critical lesions produced by a physical proton, $CL(\mathrm{LET}_{\mathrm{track}})$ is the critical lesion yield per unit track length evaluated at the track-averaged LET, and R is the physical proton range. This expression assumes that the critical lesion yield can be represented by its value at the track-averaged LET.

Since BIANCA represents each proton using the characteristic traversal length L_{cell},

the critical lesion yield is rescaled as:

$$CL_{\text{BIANCA}} = CL\left(\text{LET}_{\text{track}}\right) \cdot \frac{R}{L_{\text{cell}}} \tag{2.10}$$

where CL_{BIANCA} is the effective critical lesion yield per unit length assigned to the simulated track, $CL(\text{LET}_{\text{track}})$ is the yield associated with the physical proton track, and R/L_{cell} is the geometrical scaling factor. This correction compensates for representing a short physical track of length R by a simulated track of length L_{cell}.

The resulting mean number of critical lesions per simulated particle is:

$$N_{\text{CL}}^{\text{BIANCA}} = CL_{\text{BIANCA}} \cdot L_{\text{cell}} = CL\left(\text{LET}_{\text{track}}\right) \cdot R = N_{\text{CL}}^{\text{real}} \tag{2.11}$$

where $N_{\text{CL}}^{\text{BIANCA}}$ and $N_{\text{CL}}^{\text{real}}$ represent the mean numbers of critical lesions per simulated and physical proton, respectively. This equality demonstrates that the geometrical rescaling preserves the mean number of critical lesions associated with each proton, despite the difference between the simulated and physical track lengths.

The fragment un-rejoining probability f is evaluated at the track-averaged LET:

$$f_{\text{BIANCA}} = f\left(\text{LET}_{\text{track}}\right) = f\left(\frac{E}{R}\right) \tag{2.12}$$

where f_{BIANCA} is the fragment un-rejoining probability assigned to the simulated proton, and $f(\text{LET}_{\text{track}})$ is the corresponding radiobiological parameter evaluated at the track-averaged LET. Unlike the critical lesion yield, f is a dimensionless probability and is not geometrically rescaled.

Traversing regime

For protons capable of traversing the cell nucleus ($R \geq L_{\text{cell}}$), the standard BIANCA track-length approximation applies. The model parameters retain their unscaled values, evaluated at the initial LET (LET_0):

$$\text{LET}_{\text{BIANCA}} = \text{LET}_0, \quad CL_{\text{BIANCA}} = CL\left(\text{LET}_0\right), \quad f_{\text{BIANCA}} = f\left(\text{LET}_0\right) \tag{2.13}$$

where LET_0 is the LET corresponding to the initial kinetic energy of the proton, $CL(\text{LET}_0)$ is the critical lesion yield per unit track length at this LET, and $f(\text{LET}_0)$ is the corresponding fragment un-rejoining probability. In this regime, no geometrical correction is applied because the proton range is sufficiently large for the standard nuclear traversal approximation.

Transition region

To avoid numerical discontinuities between the stopping and traversing regimes,

a smooth interpolation is implemented around $R \approx L_{\text{cell}}$ using a weighting function w:

$$w = \frac{R - R_1}{R_2 - R_1}, \quad \text{with } R_1 = 0.7 L_{\text{cell}} \quad \text{and} \quad R_2 = 1.5 L_{\text{cell}} \tag{2.14}$$

where w is a dimensionless interpolation weight, R is the proton range, and R_1 and R_2 define the lower and upper boundaries of the transition region, respectively. The interpolation is applied for $R_1 \leq R \leq R_2$, so that $0 \leq w \leq 1$. At $R = R_1$, $w = 0$ and the short-range formulation is recovered, whereas at $R = R_2$, $w = 1$ and the standard traversing formulation is recovered.

In this transition region, the effective input parameters are evaluated as:

$$\text{LET}_{\text{BIANCA}} = (1 - w)\frac{E}{L_{\text{cell}}} + w\text{LET}_0 \tag{2.15}$$

$$CL_{\text{BIANCA}} = (1 - w)CL\left(\frac{E}{R}\right)\frac{\min(R, L_{\text{cell}})}{L_{\text{cell}}} + wCL\left(\text{LET}_0\right) \tag{2.16}$$

$$f_{\text{BIANCA}} = (1 - w)f\left(\frac{E}{R}\right) + wf\left(\text{LET}_0\right) \tag{2.17}$$

Here, $\text{LET}_{\text{BIANCA}}$, CL_{BIANCA}, and f_{BIANCA} are the effective parameters supplied to BIANCA. The weighting factor w determines the relative contributions of the short-range and traversing formulations. The term E/L_{cell} represents the effective LET of the short-range model, while LET_0 represents the initial LET used in the standard model. Similarly, $CL(E/R)$ and $f(E/R)$ are evaluated at the track-averaged LET, whereas $CL(\text{LET}_0)$ and $f(\text{LET}_0)$ correspond to the standard parameterization. The function $\min(R, L_{\text{cell}})$ selects the smaller of the physical proton range and the characteristic nuclear traversal length, limiting the geometrical correction applied to the critical lesion yield. This interpolation provides a continuous transition between the two descriptions.

2.1.6.1 Application to human skin fibroblasts (HSF)

For human skin fibroblasts (HSF), the characteristic nuclear traversal length was set to $L_{\text{cell}} = 4.0$ μm. Protons with ranges $R < 2.8$ μm, corresponding approximately to energies $E \lesssim 200$ keV, were treated using the short-range formalism. In this regime, protons were assumed to stop within the cell nucleus, and the effective BIANCA input LET was calculated as:

$$\text{LET}_{\text{BIANCA}} = \frac{E}{4.0\ \mu\text{m}} \tag{2.18}$$

where E is the initial kinetic energy of the proton and 4.0 μm is the characteristic nuclear traversal length adopted for HSF cells. The resulting $\text{LET}_{\text{BIANCA}}$ represents the

effective LET required to reproduce the proton energy deposition within the standard BIANCA track-length description.

The corresponding critical lesion yield was calculated as:

$$CL_{\mathrm{BIANCA}} = CL\left(\frac{E}{R}\right)\frac{R}{4.0\ \mu\mathrm{m}} \tag{2.19}$$

where $CL(E/R)$ is the critical lesion yield evaluated at the track-averaged LET, R is the physical proton range, and $R/(4.0\ \mu\mathrm{m})$ is the geometrical scaling factor. This correction preserves the mean number of critical lesions per proton within the short-range approximation.

Protons with $R > 6.0\ \mu$m, corresponding approximately to $E \gtrsim 400$ keV, were treated using the standard traversing regime. In this case, the input parameters are given by $\mathrm{LET}_{\mathrm{BIANCA}} = \mathrm{LET}_0$, $CL_{\mathrm{BIANCA}} = CL(\mathrm{LET}_0)$, and $f_{\mathrm{BIANCA}} = f(\mathrm{LET}_0)$, where LET_0 is the initial LET of the proton.

Finally, protons in the intermediate energy interval (200 keV $< E <$ 400 keV) were treated using the interpolation procedure. For HSF cells, the interpolation limits in Equation 2.14 were set to $R_1 = 0.7L_{\mathrm{cell}} = 2.8\ \mu$m and $R_2 = 1.5L_{\mathrm{cell}} = 6.0\ \mu$m. These boundaries define the range interval over which the effective input parameters progressively change from the short-range formulation to the standard BIANCA description.

For LET values exceeding the calibration threshold of 35 keV/μm, saturation plateaus were applied to the corresponding radiobiological parameters: $CL_{\mathrm{sat}} = 0.032$ CL/μm and $f_{\mathrm{sat}} = 0.54$. Here, CL_{sat} is the limiting critical lesion yield per unit track length, while f_{sat} is the limiting fragment un-rejoining probability.

All the resulting values are included in Table 4, highlighting the change of the track-averaged LET throughout the different regimes.

The effective-track model preserves the energy deposited per proton and the mean number of critical lesions per track in the short-range regime, under the assumption that the proton deposits its entire kinetic energy within the considered volume. However, the spatial distribution of critical lesions is approximated by distributing them along the characteristic nuclear traversal length L_{cell}, rather than restricting them to the physical stopping range R. This approximation is expected to have a limited effect when the mean number of critical lesions per proton is much smaller than unity ($CL \cdot R \ll 1$), since the probability of producing multiple critical lesions along the same proton track is then small. In the transition region, the interpolated parameters provide a continuous connection between the short-range and standard BIANCA descriptions.

2.2 Application of the extended Photon Isoeffective dose model

2.2.1 Conceptual study in a simple geometry

The extended photon isoeffective dose model was applied to a standard irradiation scenario to explore its capabilities and evaluate its relevance for Boron Neutron Capture Therapy (BNCT). The setup considers a cylindrical soft-tissue phantom irradiated by the epithermal neutron beam designed and constructed for BNCT by the Italian National Institute for Nuclear Physics (INFN) [51]. Figure 2.4, provides a schematic illustration of the main components required for the simulation and the expected outcome.

The physical characteristics of the phantom and the configuration of the irradiation source utilized to evaluate the dose distributions along the central axis are the following:

- **Phantom Dimensions:** a cylindrical phantom measuring 20 cm in diameter and 25 cm in height.
- **Material Composition:** the phantom material was modeled according to the standard elemental composition for the average soft tissue specified in ICRU Report 44 [12].
- **Irradiation Source:** the epithermal neutron beam was generated using the INFN Radio Frequency Quadrupole (RFQ) proton accelerator coupled with a beryllium target, as detailed in [51]. The beam has a circular beam port with a diameter of 14 cm. In the simulation setup, the beam port was placed directly against the top surface of the phantom, centered along its longitudinal axis.

The absorbed dose distributions as a function of LET for protons, α-particles, and carbon ions were calculated using the Particle and Heavy Ion Transport code System (PHITS) Monte Carlo based code [52]. Due to the short range of recoil carbon ions, their energy deposition was scored using the `T-Deposit` tally, and likewise employed for the secondary photon dose component, where LET-based tracking is not directly applicable to the secondary electron spectrum.

To analyze biological effectiveness in distinct tissue environments, two target volumes along the central beam axis were evaluated:

- **Superficial Region (R_1):** positioned at a shallow depth of 1 mm, where the incident neutron spectrum retains higher energies prior to significant thermalization. Physically, this region represents superficial skin tissue; therefore, the

radiobiological database established for the Human Skin Fibroblast (HSF) cell line was assigned to evaluate the dose in this volume.

- **In-Depth Region (R_2):** positioned at a depth of approximately 2.25 cm, it corresponds to the peak location of the thermal neutron flux within the phantom. Clinically, this volume models the target tumor region; thus, the radiobiological parameter database corresponding to the U-87 and SCC cell lines were applied for dose calculations in this volume.

Additionally, the energy spectrum of recoil protons generated within these two regions was scored as a function of kinetic energy using the `T-Product` tally. This scoring was conducted to assess the relative biological effectiveness of fast recoil protons compared to monoenergetic protons of 583 keV produced by the $^{14}\mathrm{N}(n,p)^{14}\mathrm{C}$ thermal neutron capture reaction.

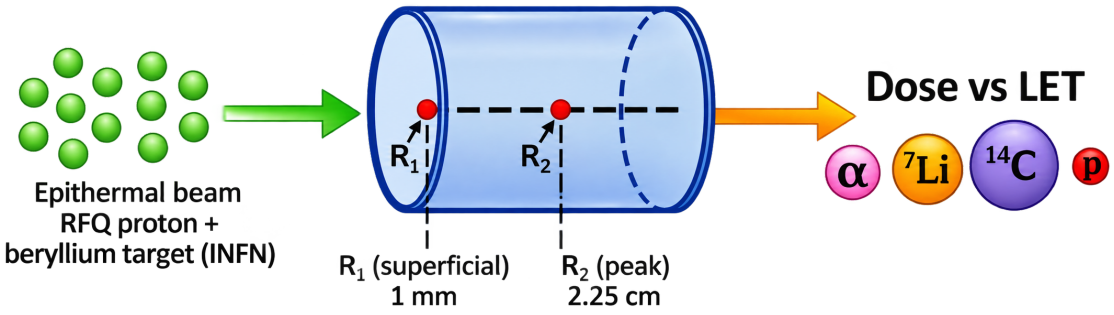


Figure 2.4: Graphical representation of the main components of the simulation, from left to right: irradiation source, cylindrical phantom and physical outcome [15].

2.2.2 Dose calculation approaches

Different formulations of the photon isoeffective dose model were evaluated in two clinical ^{10}B concentration scenarios: a normal tissue concentration (22.5 ppm) and a tumor tissue concentration (52.5 ppm). The comparative analysis evaluated two computational methodologies that vary in their level of detail regarding radiation field energy spectra and parameter energy dependence. Specifically, the original formulation of the photon isoeffective dose model was compared with that of the extended energy- and LET-dependent model.

- $\mathbf{D_{IsoE1}}$: the extended photon isoeffective dose, covered in section 1.2.4, fully represented by expression 1.19. This approach explicitly accounts for the full dependence on both the type i and energy E_{ik} (with $1 \leq k \leq N_i$) of the secondary charged particles.

- $\mathbf{D_{IsoE2}}$: the general photon isoeffective dose, as defined by expression 1.17, with the parameters α_i and β_i weighted by dose for each component of the dose of BNCT (D1, D2, D3, D4). An additional consideration in the summation is the branching ration of the nuclear capture reactions. In the case of the boron component ($i = 1$), this is:

$$\alpha = \sum_{r=1}^{2} w_r \left(\frac{\sum_{f=1}^{2} \alpha_f(E_{rf}) D_{rf}}{D_r} \right) \tag{2.20}$$

$$\beta = \sum_{r=1}^{2} w_r \left(\frac{\sum_{f=1}^{2} \sqrt{\beta_f(E_{rf})} D_{rf}}{D_r} \right) \tag{2.21}$$

where r denotes the branch of the boron neutron capture reaction, w_r the corresponding branching ratio, and and f represents the reaction products (α-particle and ^{7}Li recoil nucleus).

For the nitrogen capture reaction ($i = 2$), since there is only one reaction branch, the expressions for α_2 and $\sqrt{\beta_2}$ simplify directly to the sum of the parameter contributions of the 583 keV proton and the 42 keV carbon-14 nucleus, without the need for a summation over reaction branches.

In both boron and nitrogen capture reactions, the values of α_i and β_i are evaluated at the initial emission energies of the secondary charged particle, that is, using their initial LET values. For the recoil protons produced by the elastic scattering reaction ($i = 3$), the α_3 and $\sqrt{\beta_3}$ values are determined by considering the average LET value derived from the proton recoil spectrum scored at the corresponding position.

Chapter 3

Results and Discussion

This chapter presents the results obtained from the application of the methodology described in Chapter 2, along with a critical analysis of the findings in two main sections.

The first section focuses on the extension of pre-existing cell-specific radiobiological databases to high-LET regimes using the BIANCA model, the validation of model predictions for ion irradiation against available experimental data, and the performance testing of the short-range proton model developed for low-energy track structures.

The second section applies these generated radiobiological databases to a standard BNCT irradiation scenario to explore the capabilities of the model and evaluate its clinical relevance for Boron Neutron Capture Therapy (BNCT). The cell lines selected for evaluation correspond to representative skin models and malignant tumor models, allowing a comprehensive assessment of the radiation response in both healthy and malignant tissues.

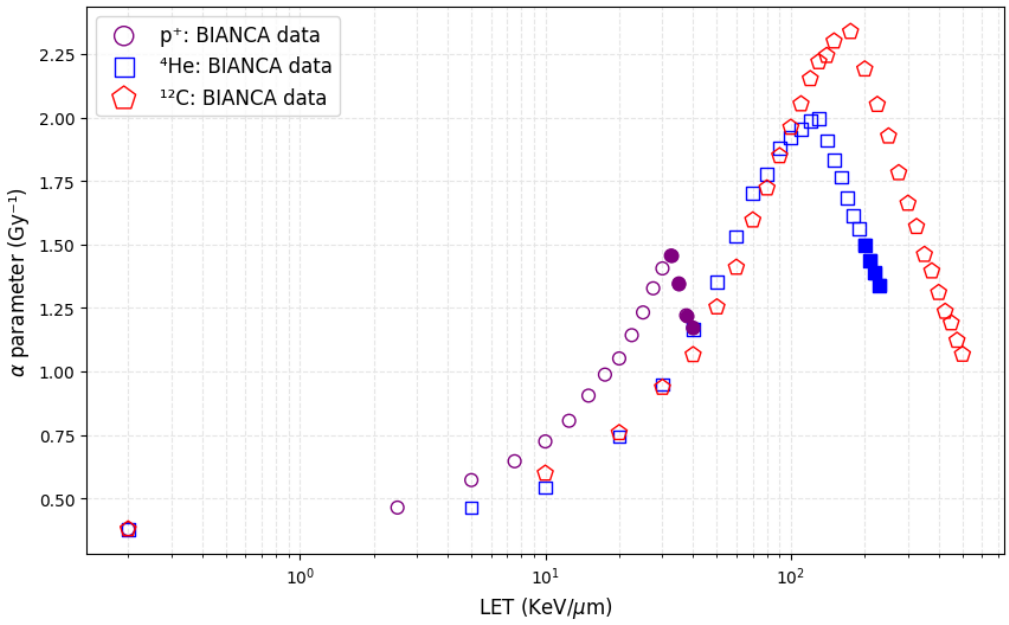
3.1 Cell-specific radiobiological parameters

3.1.1 Extension of pre-existing cell survival databases

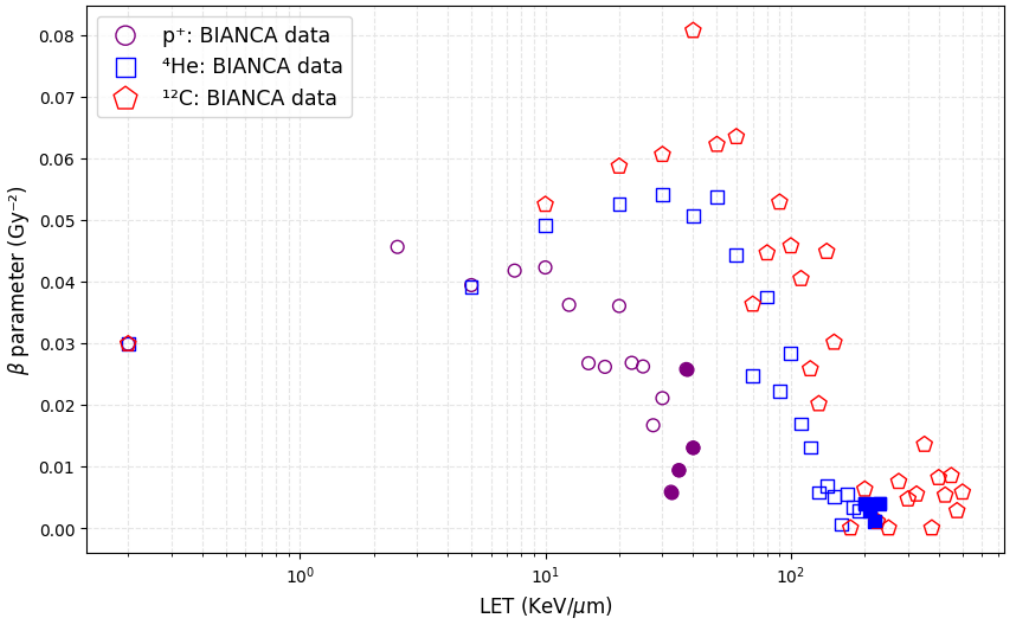
The extension of the pre-existing radiobiological databases provided the additional α and β values required to cover the LET range relevant to BNCT secondary charged particles. In this section, the results obtained for the HNSCC and HaCaT cell lines are presented, while HSF cells, for which a dedicated treatment of short-range protons was implemented, are discussed separately in Section 3.1.3.

For the HNSCC cell line, the pre-existing radiobiological database was extended by calculating additional α and β coefficients at LET values of 32.5, 35.0, 37.5, and

40.0 keV/μm for protons, and 200, 210, 220, and 230 keV/μm for helium ions. The resulting extended database is shown in Figure 3.1, where the newly generated values are indicated by filled symbols.



(a)

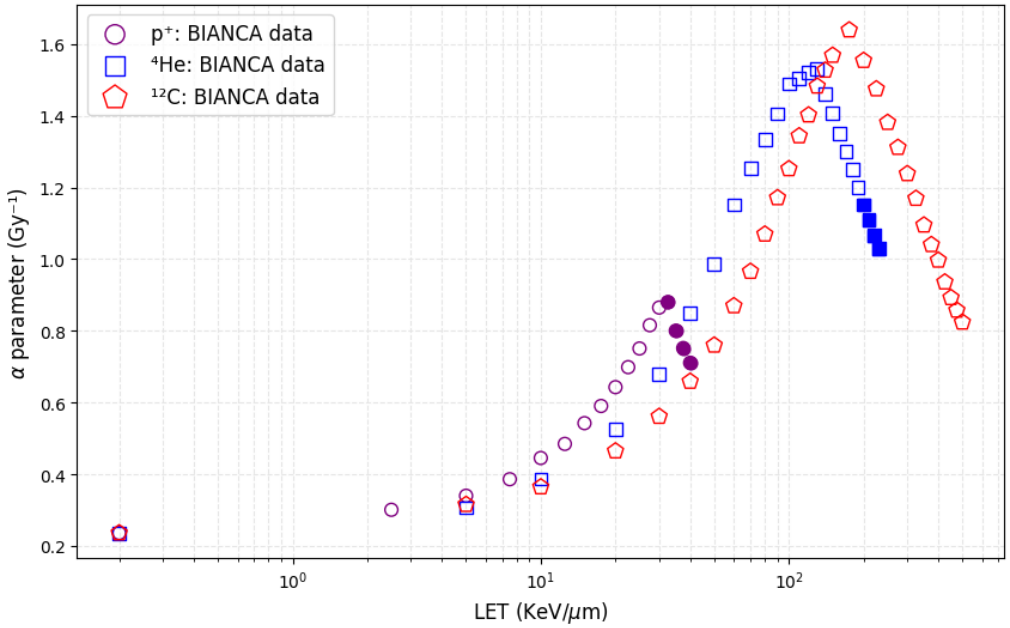


(b)

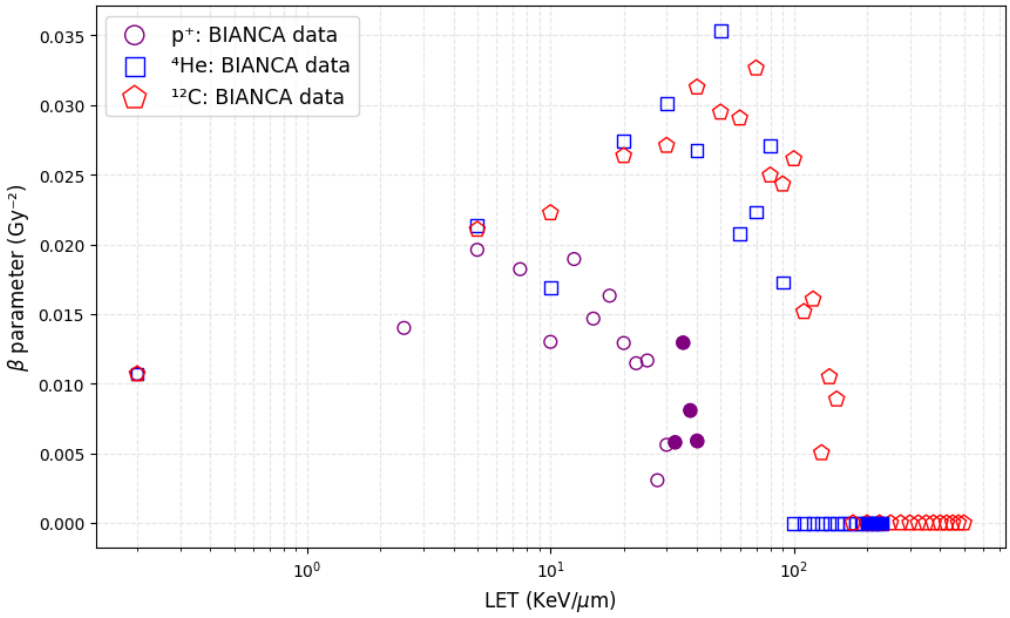
Figure 3.1: α (top) and β (bottom) coefficients as a function of LET for head and neck squamous cell carcinoma (HNSCC). Filled symbols represent the newly calculated values extending the database to the BNCT-relevant LET range.

The same extension was performed for the HaCaT cell line. Additional α and β

coefficients were calculated at LET values of 32.5, 35.0, 37.5, and 40.0 keV/μm for protons, and 200, 210, 220, and 230 keV/μm for helium ions. The resulting extended radiobiological database is shown in Figure 3.2.



(a)



(b)

Figure 3.2: α (top) and β (bottom) coefficients as a function of LET for immortalized human keratinocytes (HaCaT). Filled symbols represent the newly calculated values extending the database to the BNCT-relevant LET range.

The extended HNSCC and HaCaT databases show similar overall trends in the LET

dependence of the radiobiological parameters. These trends are discussed below, with particular attention to the behavior of the α and β coefficients and their dependence on particle type.

The coefficients α (Figures 3.1a and 3.2a) initially increase with LET, reach a maximum, and subsequently decrease, regardless of the cell line. This characteristic behavior is associated with the overkill effect, in which additional energy deposition within a single particle track no longer yields a proportional increase in biological damage. At very high LET, fewer particle tracks are required to deliver the same absorbed dose, while the damage produced by an individual track is already close to saturation. Consequently, the biological effectiveness per unit dose decreases, leading to the observed reduction in α beyond its maximum.

The maximum occurs at different LET values for each particle species, at approximately 30 keV/μm for protons, 130 keV/μm for helium ions, and 150 keV/μm for carbon ions. This ion-dependent variation arises because light ions at high LET possess a lower kinetic energy per nucleon, resulting in narrow track cores with extremely dense local ionization. In contrast, heavier ions at the same LET distribute a larger fraction of their energy over wider δ-ray penumbras, causing protons to reach the overkill region at lower LET values.

Within the BIANCA framework, this behavior is related to the interplay between the induction of critical lesions, described by the parameter CL, and the probability of chromosome fragment un-rejoining, described by f. Both parameters may increase with LET until reaching their respective saturation values, $CL_{\max}$ and $f_{\max}$ [32]. Once these saturation regimes are reached, a further increase in LET does not lead to a proportional increase in the biological damage produced per particle track. At the same time, the number of particle tracks required to deliver a given absorbed dose decreases with increasing LET, contributing to the reduction in α observed in the overkill region.

In contrast, the parameter β (Figures 3.1b and 3.2b) does not exhibit a well-defined dependence on LET, showing considerable scatter throughout the LET range of interest. At high LET values, the linear-quadratic fits of the BIANCA-predicted survival curves generally yield small β values. Whenever an unconstrained linear-quadratic fit produced a negative value, β was constrained to zero ($\beta = 0$), since negative values are not physically meaningful within the LQ model.

3.1.2 Generation and validation of the U-87 radiobiological database

Following the methodology detailed in Section 2.1.5, the construction of the database begins by establishing the baseline cell survival response under reference photon irradiation as a function of absorbed dose. The experimental cell survival data set for ^{60}Co

γ-ray irradiation taken from Marcaccio et al. [47] was used to calibrate the BIANCA parameters CL and f, obtaining a cluster lesion yield of $CL = 1.75$ CL/(Gy $\cdot$ cell) and an unrejoining probability of $f = 0.092$. These optimal CL and f parameters that best fit the experimental data were determined through a trail and error process that compared the radiobiological parameters α and β resulting from a series of BIANCA simulations against the values of the literature.

Figure 3.3 illustrates the cell survival curves for the U-87 glioblastoma cell line exposed to the various photon reference radiations. The spread observed across these datasets highlights the inherent biological and experimental variability in clonogenic assays even when using the same nominal cell line (U-87), as there may be differences in culture conditions, cell passage number, etc. Additionally, because the Marcaccio et al. curve lies centrally between the extreme responses reported in the literature, it avoids introducing systematic bias into the intrinsic cell parameters (CL and f) since it represents a median central-tendency response for the U-87 line in the literature.

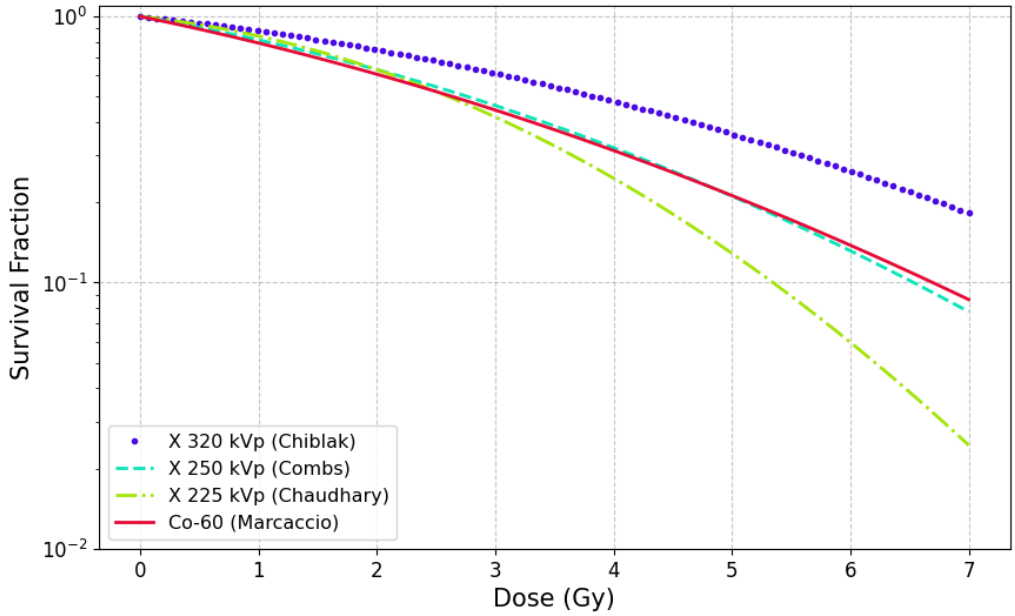
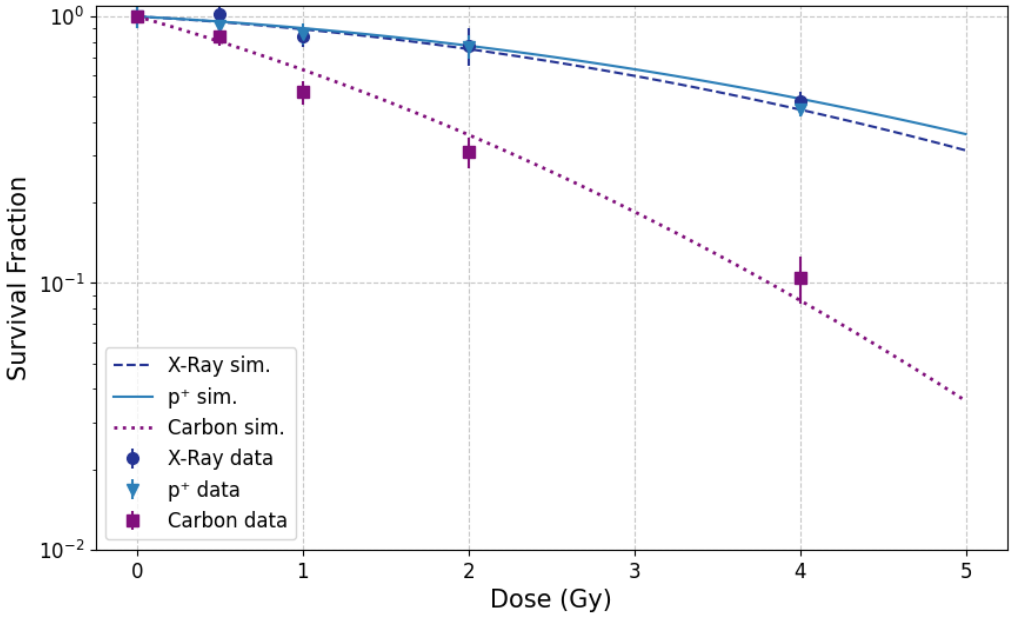


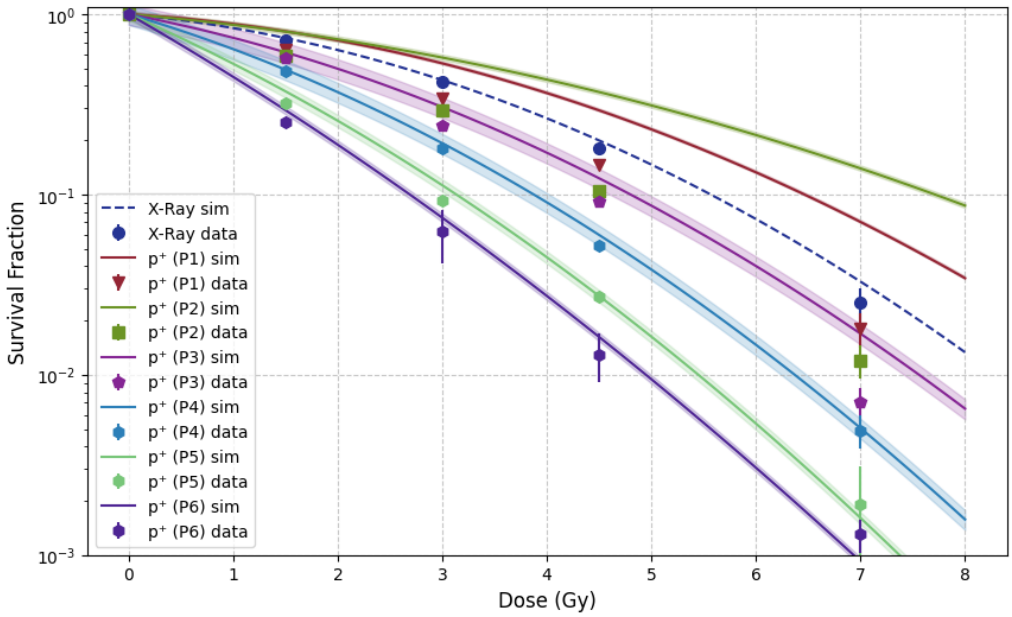
Figure 3.3: comparison of the survival fraction between the different photon irradiations of the selected experimental datasets.

To assess and evaluate the predictive capacity of the BIANCA model across different ions, the simulation results were validated against independent published experimental cell survival datasets for U-87 cells exposed to proton and carbon-ion beams.

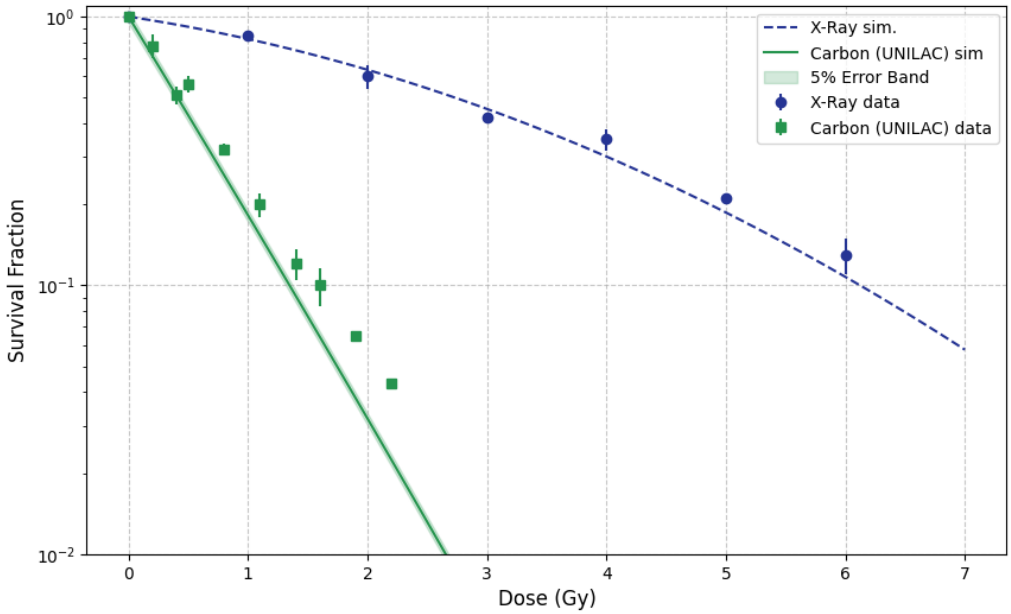
Based on the description of the selected experimental datasets provided in Section 2.1.5, Figure 3.4 illustrates the comparison between the published experimental cell survival data and the predictions generated by the BIANCA model.



(a) experimental data (symbols) and BIANCA predictions (lines) for U-87 cell survival as a function of absorbed dose for X-rays, protons, and carbon ions [48].



(b) experimental data (symbols) and BIANCA predictions (lines) for U-87 cell survival at irradiation positions P1–P6 along the 62-MeV proton beam [50].



(c) experimental data (symbols) and BIANCA predictions (lines) for U-87 cell survival as a function of absorbed dose for X-rays and monoenergetic carbon-ion irradiation [49].

Figure 3.4: comparison between experimental U-87 cell survival data and BIANCA predictions for proton and carbon-ion irradiation.

Under proton irradiation, the agreement between the BIANCA predictions and the experimental data depends on the dataset considered. For the experimental data shown in Figure 3.4a, corresponding to proton irradiation at an LET of approximately 2.5 keV/μm, the BIANCA prediction is in good agreement with the measured cell survival data.

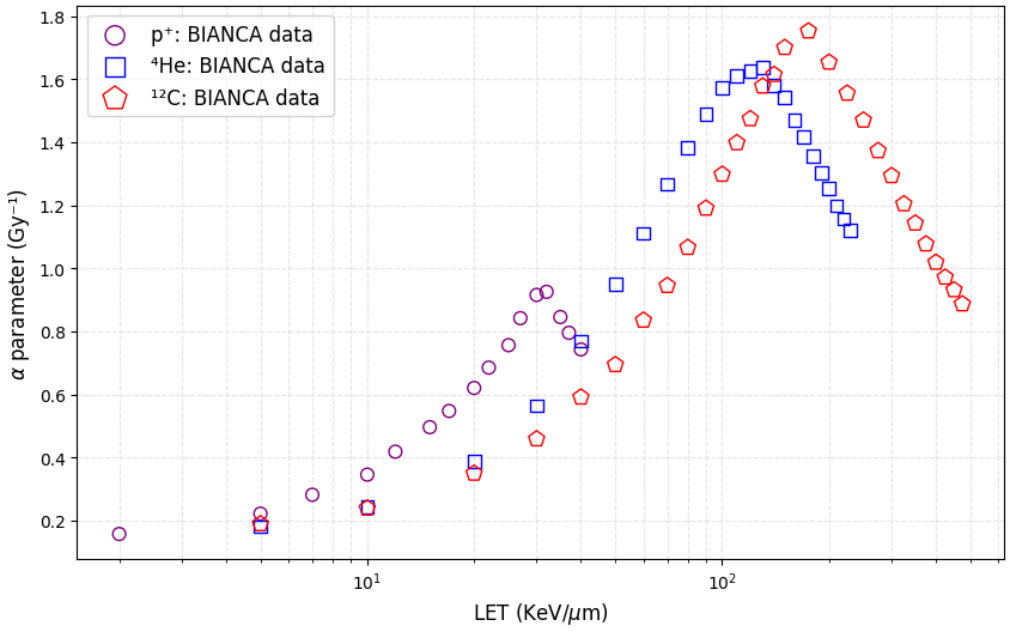
A different behavior is observed for the experimental data reported by Chaudhary et al. [50] and shown in Figure 3.4b. In this experiment, U-87 cells were irradiated at six positions (P1–P6) along a 62-MeV proton beam, corresponding to increasing dose-averaged LET values of approximately 1.1, 4.0, 7.0, 11.9, 18.0, and 22.6 keV/μm, respectively. At the first positions, particularly in the low-LET region, an offset is observed between the BIANCA predictions and the experimental survival data. This discrepancy cannot be attributed solely to LET, since good agreement is obtained with the independent proton dataset at 2.5 keV/μm shown in Figure 3.4a. At increasing LET values, BIANCA reproduces the progressive increase in cell killing observed experimentally along the proton beam.

For carbon-ion irradiation, the BIANCA predictions are generally in good agreement with the available experimental data. In Figure 3.4a, the predicted survival curve for carbon ions at approximately 40 keV/μm reproduces the experimental survival response reported in the corresponding dataset. In Figure 3.4c, corresponding to monoenergetic carbon-ion irradiation at approximately 170 keV/μm, the BIANCA

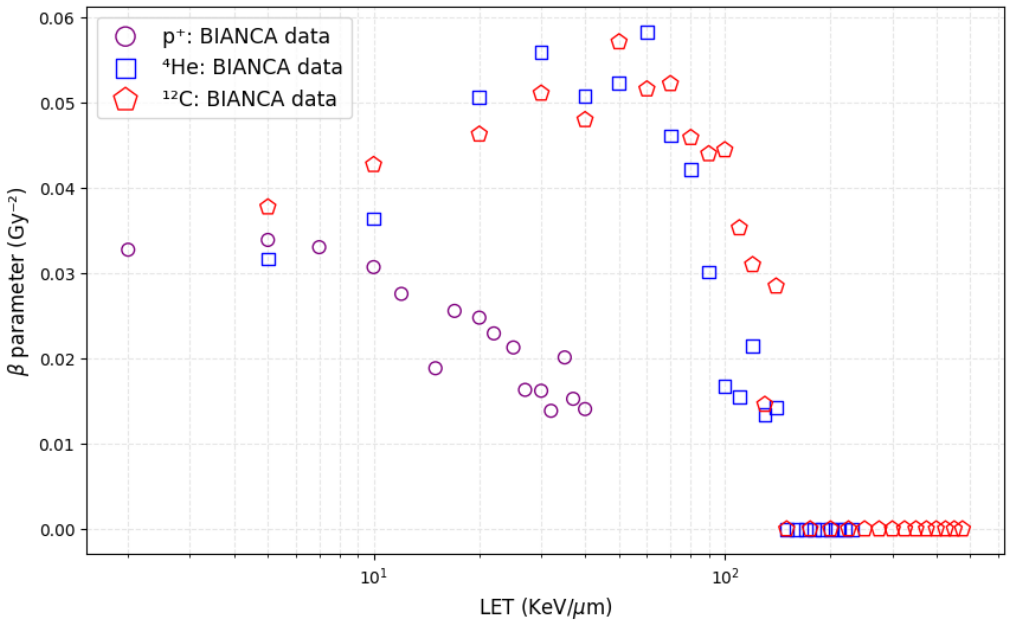
prediction closely reproduces the experimental survival response up to approximately 1.5 Gy. At higher doses ($>$ 2 Gy), the experimental survival fractions are slightly higher than those predicted by the model.

Overall, the comparison with independent ion-irradiation datasets shows that the BIANCA parameterization derived from the reference photon response is able to reproduce the main features of the U-87 response to proton and carbon-ion irradiation over a broad LET range, although some dataset-dependent discrepancies are observed, particularly for the low-LET proton data reported by Chaudhary et al. [50].

Once the validation of the BIANCA model against published experimental data was complete, the construction of the extended cell-survival database was carried out for the U-87 glioblastoma cell . Following the methodology described in Section 2.1.5, the Linear-Quadratic parameters α and β were derived for each ion species across their respective LET ranges, as shown in Figure 3.5 and collected in Table 5.



(a)



(b)

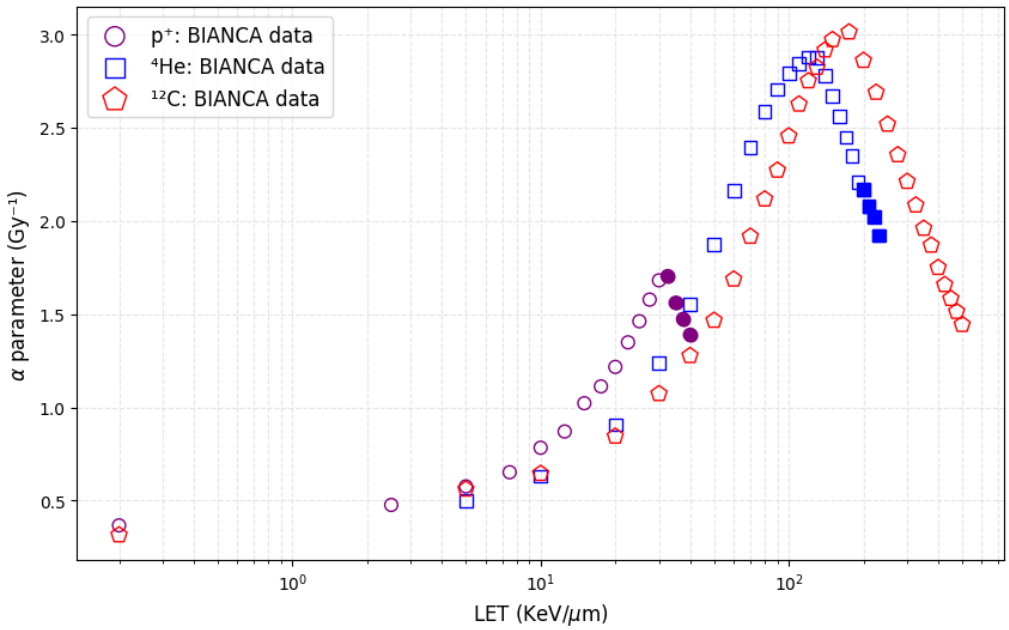
Figure 3.5: α (top) and β (bottom) coefficients as a function of LET for U87 cells.

The LET dependence of parameters α and β for U-87 cells closely mirrors the behavior observed for the cell lines evaluated previously. In Figure 3.5a, the parameter α displays the characteristic overkill effect, reaching a maximum and subsequently decreasing at higher LET values. The position of this maximum depends on the ion species.

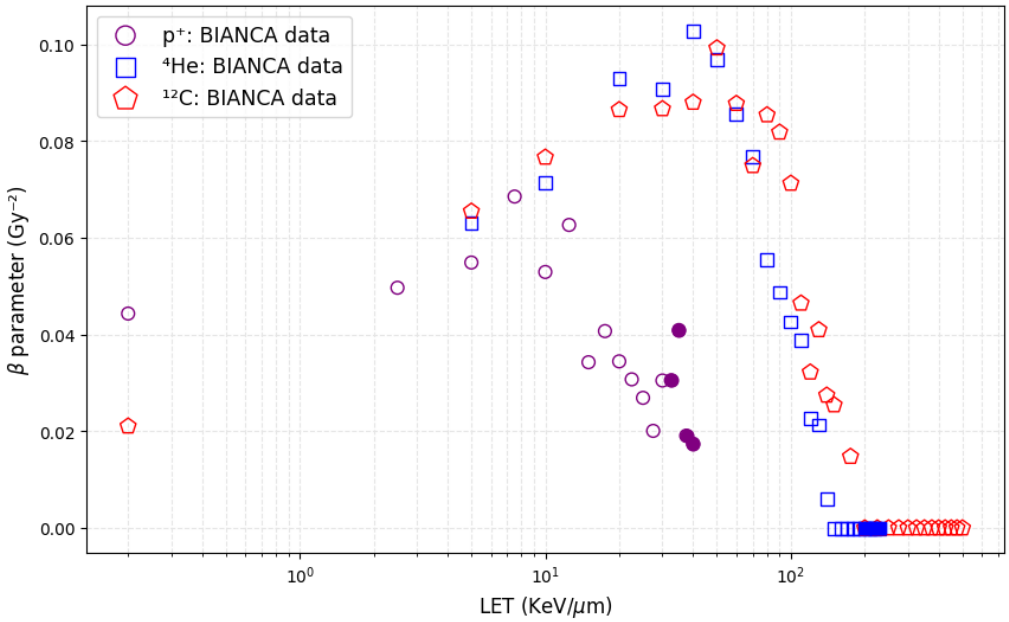
In contrast, as shown in Figure 3.5b, the quadratic parameter β does not exhibit a well-defined trend with LET. At elevated LET values, whenever the unconstrained fits yielded negative values, β was constrained to zero ($\beta = 0$), since negative values are not physically meaningful within the LQ model.

3.1.3 Short-range proton modeling in HSF cells

Before evaluating the biological impact of low-energy secondary protons, the pre-existing cell survival database for human skin fibroblasts (HSF) was extended across the LET ranges relevant to BNCT (up to 40 keV/μm for protons and 230 keV/μm for helium ions). The derived radiobiological parameters are presented in Figure 3.6.



(a)



(b)

Figure 3.6: α (top) and β (bottom) coefficients as a function of LET for human skin fibroblasts (HSF). Filled symbols represent the newly calculated values extending the database to the BNCT-relevant LET range.

The trends observed for the parameters α and β are consistent with those previously described for the other cell lines in the preceding Sections 3.1.1 and 3.1.2.

To account for the localized energy deposition of low-energy, short-range protons, the procedure described in Section 2.1.6.1 was implemented. This procedure provides

the BIANCA parameters CL and f required to perform simulations in the short-range, transition, and fully traversing regimes. Cell survival fractions generated directly by BIANCA were fitted using the Linear-Quadratic model to extract the radiobiological parameters α and β.

Since, in the low-energy region, different proton energies can correspond to the same LET value, the new radiobiological database was constructed as a function of proton kinetic energy. To combine the results obtained using the short-range proton treatment developed in this thesis with the pre-existing BIANCA database, the LET values of the latter were converted into kinetic energy using the proton stopping-power and range tables provided by NIST [53]. This resulted in an energy-dependent database covering proton energies from 1 keV to 200 MeV.

Figure 3.7 shows the resulting α values for the different proton transport regimes: short-range, transition, and fully traversing. To maintain consistency with the databases presented in the previous sections, the results are plotted as a function of track-averaged LET, while the corresponding proton energies are indicated in the figure. The three regimes correspond to $E \lesssim 200$ keV for short-range protons, 200 keV $< E <$ 400 keV for the transition region, and $E \gtrsim 400$ keV for protons that fully traverse the nucleus. Only the α parameter is shown, since β does not show a significant deviation from the behavior observed in the high-energy database (Figure 3.6b).

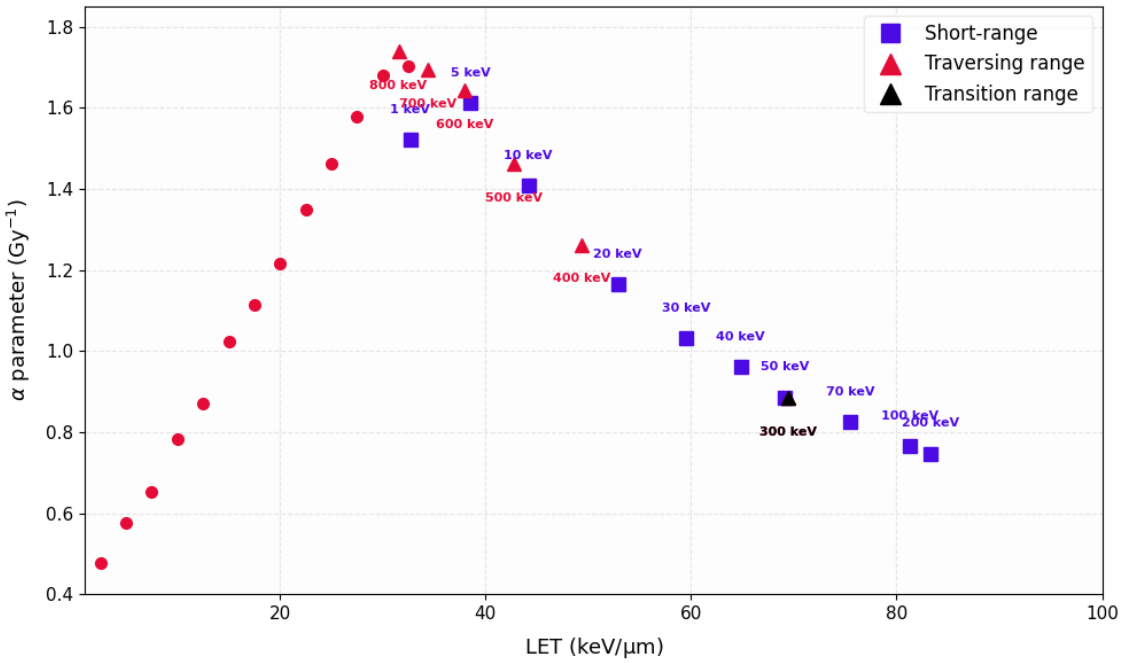


Figure 3.7: α coefficients as a function of the track-averaged LET for Human Skin Fibroblast (HSF) in the different regimes.

In the fully traversing regime ($E \gtrsim 400$ keV), α shows the characteristic depen-

dence on LET already observed for the other cell lines, increasing with LET and subsequently decreasing as the overkill region is approached. In this regime, the proton range is sufficiently large to completely traverse the nucleus, and the calculated α values follow the behavior obtained with the standard BIANCA treatment. The point corresponding to the transition region (200 keV $< E <$ 400 keV) continues the trend observed toward lower proton energies.

For short-range protons ($E \lesssim 200$ keV), a different behavior is observed: as the proton energy decreases, the track-averaged LET (E/R) also decreases, contrary to the trend generally observed at higher proton energies. Since these protons are in the overkill region, where α decreases with increasing LET, the reduction in LET is accompanied by an increase in α. This behavior highlights the importance of accounting for the specific energy dependence of LET in short-range protons when evaluating their radiobiological effectiveness.

3.2 Evaluation of the photon isoeffective dose

To evaluate the impact of the different approximations used in the calculation of the photon isoeffective dose, the two regions of interest defined in Section 2.2.1 were considered: a superficial region (R_1), representing healthy tissue, and a deeper region (R_2), representing tumor tissue. The results are presented and discussed separately for each region.

3.2.1 Healthy tissue region

The contribution of secondary protons was investigated in the superficial tissue region (R_1), at a depth of 1.1 mm, using radiobiological parameters corresponding to human skin fibroblasts (HSF), representing healthy skin tissue. A boron concentration of 22.5 ppm was considered, corresponding to a blood boron concentration multiplied by a tissue-to-blood concentration ratio of 1.5. Blood boron concentrations during BNCT typically range from 10 to 30 ppm, depending on the boron carrier and the time of irradiation [54]. Following the assumptions adopted in [23], the blood boron concentration considered was 15 ppm.

As described in Section 2.2.1, secondary proton production was scored as a function of kinetic energy using the T-Product tally. Figure 3.8 shows the energy spectrum of secondary protons produced at a depth of 1.1 mm. A sharp peak is observed at approximately 583 keV, corresponding to protons produced by the thermal neutron capture reaction $^{14}\mathrm{N}(n,p)^{14}\mathrm{C}$. The remaining continuous spectrum is associated with recoil protons generated by elastic scattering of neutrons with hydrogen nuclei

(^{1}H$(n,n)p$), covering a broad range of kinetic energies.

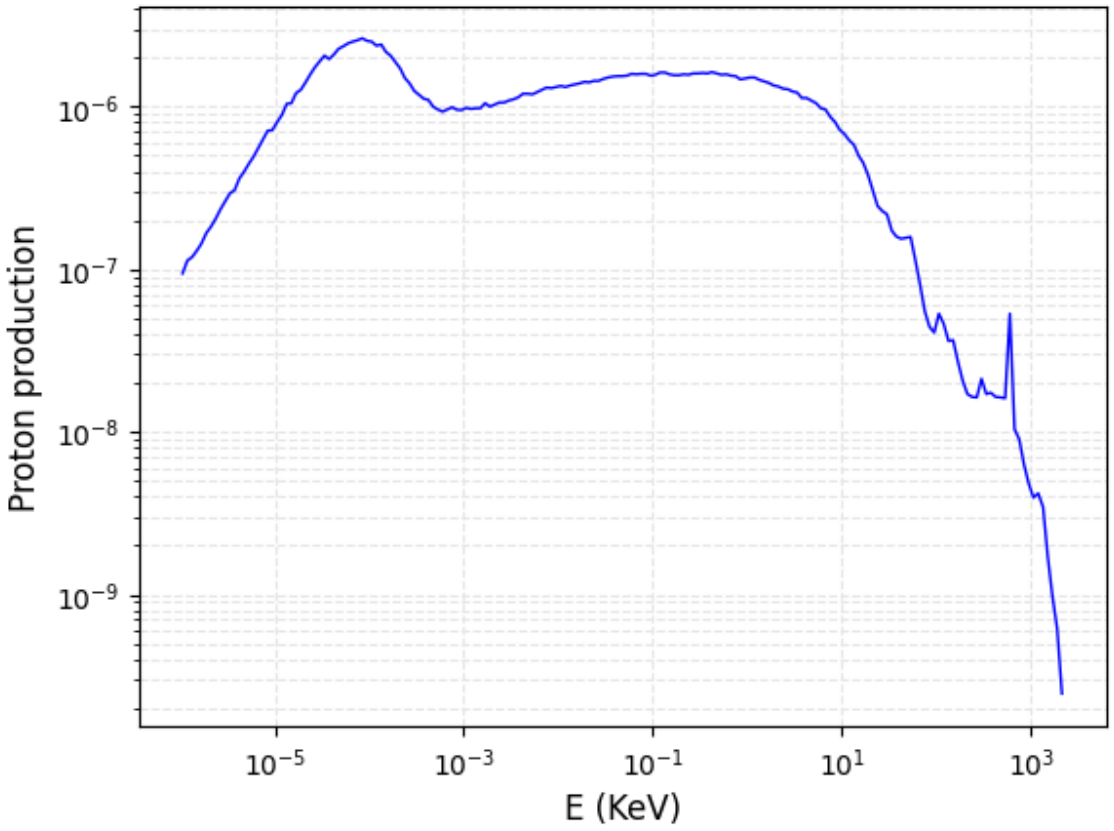


Figure 3.8: proton production as a function of kinetic energy at a superficial depth of 1.1 mm (region R_1).

The spectrum shows a significant secondary bump at very low energies ($\sim 10^{-5}$ to 10^{-3} keV). Although these ultra-low-energy particles contribute minimally to macroscopic absorbed dose due to their low kinetic energy, as will be described below, they represent a high fluence of particles that stop within micromete or even nanometer distances. Moreover, a substantial population of protons generated falls below 200 keV, where the physical range ($R \leq 2.8\ \mu$m) is strictly smaller than the HSF nuclear diameter ($L_{\text{cell}} = 4.0\ \mu$m). This high fluence of short-range protons highlights the importance of incorporating a dedicated treatment for short-range protons within BIANCA.

To evaluate the contribution of secondary protons to the absorbed dose, the proton dose distribution as a function of kinetic energy is shown in Figure 3.9. Similarly to the production spectrum, a prominent peak is observed at approximately 583 keV, corresponding to protons produced by the ^{14}N$(n,p)^{14}$C reaction. In addition to this discrete peak, the continuous recoil proton spectrum accounts for a substantial fraction of the total proton dose, with significant contributions from protons with kinetic energies ranging from approximately 1 keV to 2 MeV.

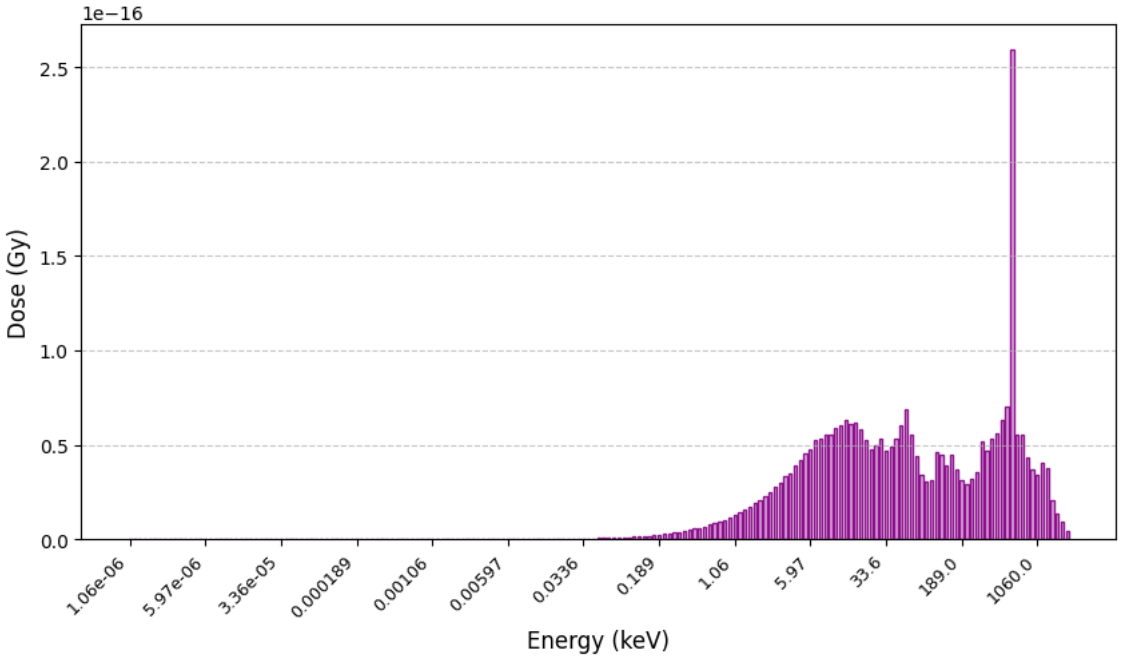


Figure 3.9: dose imparted by secondary protons as a function of kinetic energy at 1.1 mm depth (region R_1).

Unlike the proton production spectrum, the dose distribution shows very small contributions at energies below approximately 0.1 keV, indicating that the large number of protons produced at extremely low energies does not necessarily translate into a significant contribution to the absorbed dose. Furthermore, the broad energy distribution of recoil protons, including particles with ranges shorter than the characteristic nuclear dimension, motivates the use of energy-dependent radiobiological parameters in the calculation of the photon isoeffective dose.

The relative contribution of each BNCT dose component to the total absorbed dose at a depth of 1.1 mm is illustrated in Figure 3.10. In superficial normal tissue, fast neutron elastic scattering (recoil protons) and the photon component represent the dominant dose contributions, each accounting for approximately 36% of the total absorbed dose. The boron capture component ($^{10}\mathrm{B}(n,\alpha)^{7}\mathrm{Li}$) contributes approximately 25%, while neutron capture on nitrogen ($^{14}\mathrm{N}(n,p)^{14}\mathrm{C}$) contributes around 3%. The substantial contribution of recoil protons to the total absorbed dose highlights the importance of accurately accounting for their energy-dependent radiobiological effectiveness in the calculation of the photon isoeffective dose.

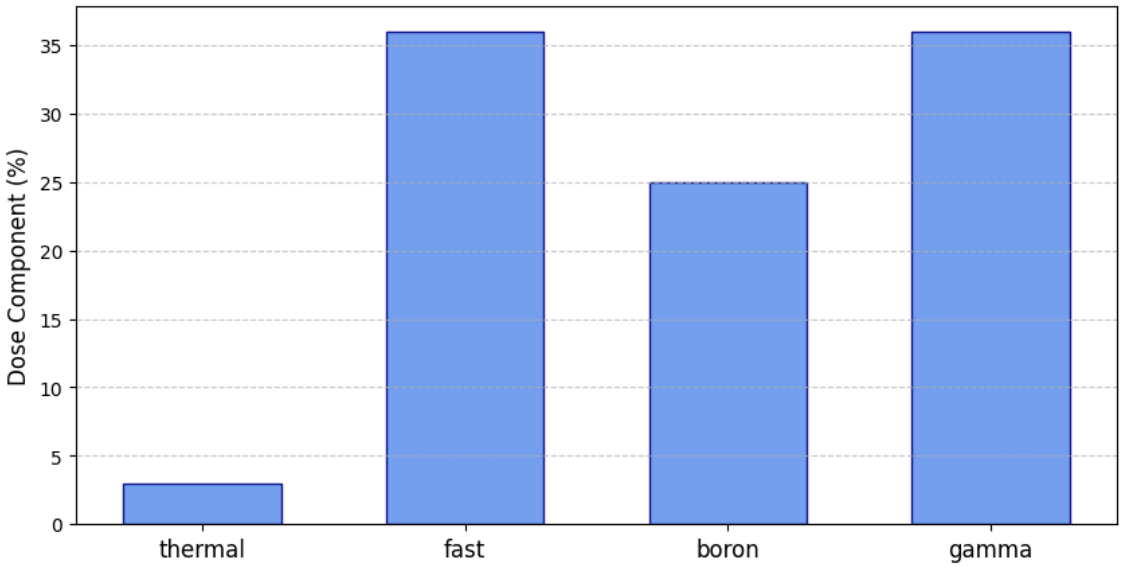


Figure 3.10: relative contribution of individual dose components to the total absorbed dose at 1.1 mm depth in region R_1 (^{10}B concentration of 22.5 ppm).

Using the energy-dependent radiobiological parameters generated for BNCT secondary particles, the extended photon isoeffective dose (D_{IsoE1}) was calculated and compared with the dose-component-based approach (D_{IsoE2}), as described in Section 2.2.2. Figure 3.11 presents both photon isoeffective dose curves and their relative percentage difference as a function of total absorbed dose. The percentage difference was calculated as:

$$\text{Relative Difference (\%)} = \frac{D_{\mathrm{IsoE2}} - D_{\mathrm{IsoE1}}}{D_{\mathrm{IsoE1}}} \times 100. \tag{3.1}$$

As shown in Figure 3.11, D_{IsoE2} systematically yields higher photon isoeffective dose values than D_{IsoE1} over the entire absorbed dose range considered. At low absorbed doses ($\sim$ 1 Gy), the relative difference reaches approximately 5.5%, gradually decreasing to around 4.8% at 30 Gy. For the same physical absorbed dose, the lower photon isoeffective dose predicted by D_{IsoE1} corresponds to a lower estimated biological effect in healthy tissue. Such a result may have implications for the estimation of normal tissue toxicity and the evaluation of dose constraints in BNCT treatment planning.

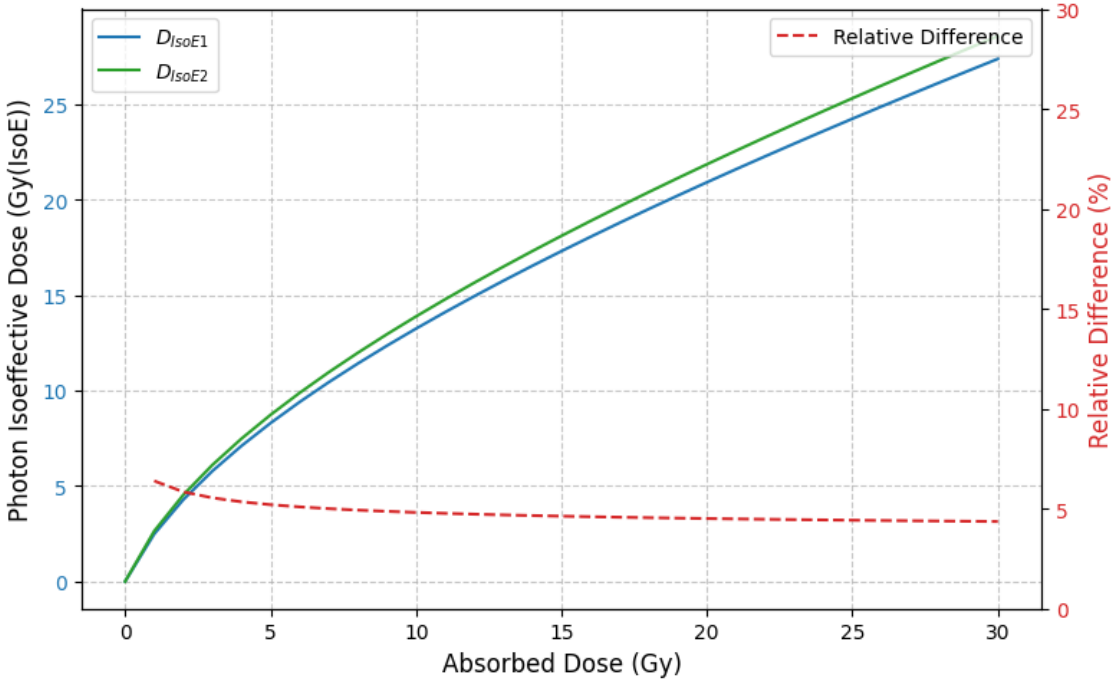


Figure 3.11: comparison between the extended photon isoeffective dose (D_{IsoE1}) and the dose-component-based approximation (D_{IsoE2}) for HSF cells in region R_1 (1.1 mm depth), including their relative percentage difference as a function of total absorbed dose.

The observed discrepancy may be partly attributed to the treatment of recoil protons, which represent a substantial fraction of the absorbed dose in this region. While D_{IsoE2} uses radiobiological parameters associated with an average LET for recoil protons, D_{IsoE1} explicitly accounts for their energy distribution and the corresponding variation in radiobiological effectiveness. In particular, the explicit treatment of short-range protons described in Section 3.1.3 may contribute to the lower photon isoeffective dose obtained with the extended formulation, although the contributions of other secondary particles may also play a role.

3.2.2 Tumor tissue region

Subsequently, the analysis was extended to the region R_2, representing tumor tissue at greater depth. A boron concentration of 52.5 ppm was assumed for the tumor, corresponding to a tumor-to-blood concentration ratio of 3.5 and a blood boron concentration of 15 ppm, following the agreement established in the previous section. Figure 3.12 shows the relative contributions of the different components of the BNCT dose to the total dose absorbed in this region.

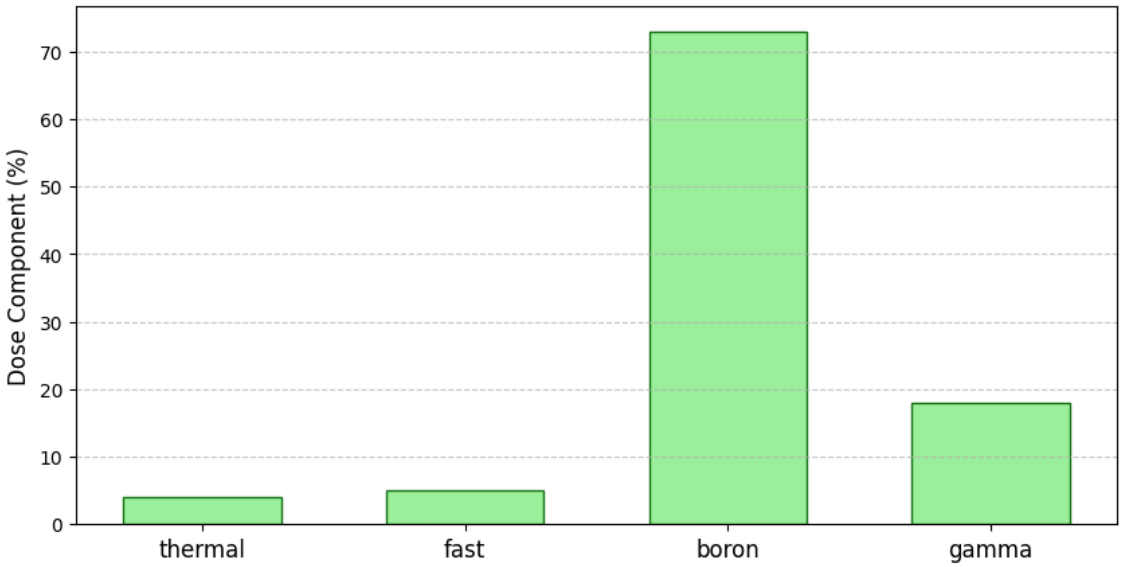
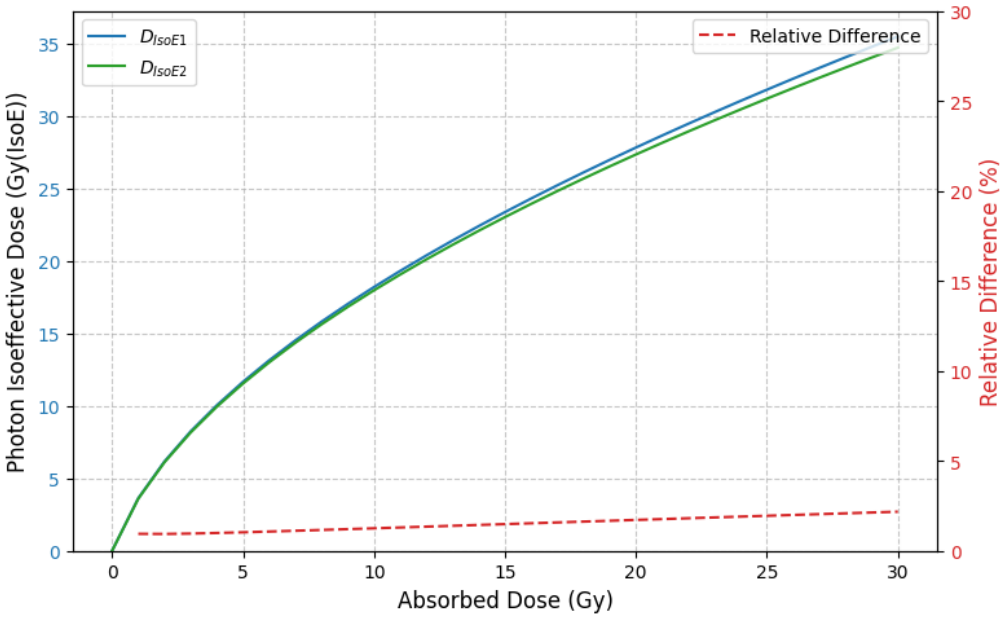


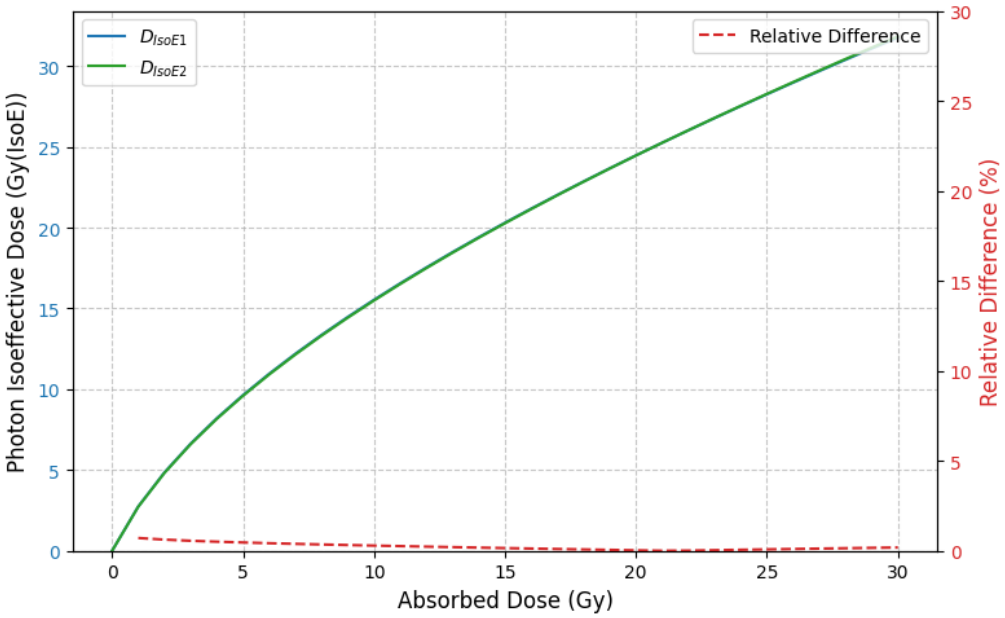
Figure 3.12: relative contribution of individual dose components to the total absorbed dose at 2.25 cm depth in region R_2 (^{10}B concentration of 52.5 ppm).

The neutron boron reaction provides the largest contribution to the total absorbed dose, reflecting both the elevated ^{10}B accumulation (52.5 ppm) and the thermalization peak of the epithermal neutron flux within the phantom. In contrast, recoil protons account for approximately 5% of the absorbed dose, considerably less than the 36% observed in the superficial healthy tissue region (R_1). This reduction confirms effective neutron moderation along the beam trajectory, shifting the primary mechanism of cell damage from fast recoil protons to thermal neutron capture products. Moreover, this difference between the two regions of interest reflects the different composition of the radiation field and the greater relative importance of the boron dose component in R_2 (73%).

Because high-LET particles from boron decay (α and ^{7}Li) dominate the physical dose distribution in R_2, the overall biological effect is primarily governed by heavy short-range charged particles. The direct consequence of this can be observed in the Photon Isoeffective Dose calculation, in which both approaches were obtained and then compared using the radiobiological parameters generated for the two tumor cell lines, U-87 glioblastoma and HNSCC. Figure 3.13 presents the results obtained with the extended formulation (D_{IsoE1}) and the dose-component-based approximation (D_{IsoE2}) for both cell lines, along with their relative percentage differences as a function of total absorbed dose.



(a)



(b)

Figure 3.13: comparison between the extended photon isoeffective dose (D_{IsoE1}) and the dose-component-based approximation (D_{IsoE2}) for (a) U-87 and (b) HNSCC cells in region R_2 (2.25 cm depth), including their relative percentage difference as a function of total absorbed dose. In panel (b), the two curves almost completely overlap, making the blue curve difficult to distinguish.

In contrast to the superficial healthy tissue layer (R_1), both tumour cell lines demonstrate strong agreement between D_{IsoE1} and D_{IsoE2}. This convergence is physically ex-

plained by the dominance of the boron capture reaction (^{10}B$(n,\alpha)^{7}$Li), as mentioned above, it constitutes $\sim$ 73% of the total physical dose at R_2.

For U-87 glioblastoma cells (Figure 3.13a), D_{IsoE1} yields slightly higher isoeffective doses than D_{IsoE2}, with a relative difference rising from $\sim$ 1.0% at low doses to approximately 2.2% at 30 Gy. This indicates that, for the same physical absorbed dose, the extended formulation predicts a slightly greater biological effect in tumour cells compared with the dose-component-based approximation. For HNSCC cells (Figure 3.13b), the agreement is even closer, with relative differences remaining below 0.8% across the entire 0–30 Gy range. These results indicate that while the detailed energy-dependent model (D_{IsoE1}) is critical in healthy superficial tissue dominated by unmoderated recoil protons, the reaction-weighted approximation (D_{IsoE2}) provides an excellent representation of biological effectiveness in boron-rich tumour regions.

It is important to emphasize that this analysis represents a case study illustrating the application of the generated radiobiological databases to BNCT dose calculations. The main contribution of this work lies in the generation and extension of cell-specific radiobiological parameters, which can subsequently be applied to more realistic BNCT irradiation scenarios, considering different irradiation conditions and tissue characteristics.

Chapter 4

Conclusions

This thesis investigated the use of the BIANCA biophysical model to generate energy-dependent radiobiological parameters for secondary charged particles produced in Boron Neutron Capture Therapy (BNCT), and their application within the extended Photon Isoeffective Dose model. Particular attention was devoted to extending cell-specific radiobiological databases and developing a treatment for low-energy, short-range protons.

Radiobiological databases were generated or extended for human skin fibroblasts (HSF), immortalized human keratinocytes (HaCaT), head and neck squamous cell carcinoma (HNSCC), and U-87 glioblastoma cells. Using BIANCA, the corresponding linear-quadratic parameters α and β were calculated for different charged particles. Existing databases were extended up to LET values of 40 keV/μm for protons and 230 keV/μm for helium ions, covering the radiation qualities associated with protons from the $^{14}\mathrm{N}(n,p)^{14}\mathrm{C}$ reaction and alpha particles from the $^{10}\mathrm{B}(n,\alpha)^{7}\mathrm{Li}$ reaction. The calculated α coefficients generally increased with LET before reaching a particle-dependent maximum and subsequently decreasing due to the *overkill* effect. In contrast, β showed a less systematic LET dependence and tended to become small at high LET values.

For U-87 cells, a new radiobiological database was generated by calibrating BIANCA against experimental photon survival data. Comparisons with published proton and carbon-ion irradiation results showed that the model reproduced the main trends in radiobiological response.

A major methodological contribution was the development of an energy-dependent treatment for short-range protons, particularly relevant to recoil protons produced by elastic neutron scattering on hydrogen. At low energies, protons with different energies may have the same LET but substantially different ranges, making LET alone insufficient to characterize their interaction with the cell nucleus. For proton ranges

smaller than the characteristic nuclear dimension, an effective LET was defined as the ratio between the initial proton energy and this dimension, and the BIANCA parameters were adapted to account for the limited track length. Application to HSF cells showed that the α coefficient increases as proton energy decreases, even when the effective LET decreases, highlighting the importance of explicitly considering particle range in radiobiological predictions.

The generated radiobiological parameters were subsequently applied to Photon Isoeffective Dose calculations in a simplified BNCT irradiation scenario, considering superficial healthy tissue and a deeper tumour region. Two approaches were compared: the extended formulation (D_{IsoE1}), which explicitly accounts for the energy dependence of secondary charged particles, and a dose-component-based approximation (D_{IsoE2}).

In the superficial healthy tissue region, recoil protons from elastic neutron scattering on hydrogen contributed substantially to the total absorbed dose, emphasizing the importance of their energy distribution and radiobiological effectiveness. For HSF cells, D_{IsoE2} systematically predicted higher values than D_{IsoE1}, with relative differences ranging from approximately 5.5% at low absorbed doses to 4.8% at 30 Gy. This corresponds to a lower predicted biological effect with the extended formulation for the same absorbed dose. The difference may be partly associated with its explicit treatment of the energy-dependent effectiveness of recoil protons, including short-range particles.

In the tumour region (R_2), the comparison between the two Photon Isoeffective Dose approaches showed smaller differences, remaining below 2.2% for U-87 cells. Over most of the investigated absorbed dose range, D_{IsoE1} was slightly higher than D_{IsoE2}, indicating that the extended formulation predicts a slightly greater biological effect for the same physical absorbed dose.

These results indicate that the impact of explicitly accounting for particle energy depends on both the composition of the mixed radiation field and the radiobiological characteristics of the irradiated cell line. In particular, the differences between the two Photon Isoeffective Dose approaches were more pronounced in the superficial healthy tissue region than in the tumour region. This suggests that the relevance of energy-dependent radiobiological parameters may vary across different irradiation conditions and tissue types. Consequently, their inclusion may be particularly important in regions where secondary charged particles exhibit broad energy distributions and contribute substantially to the absorbed dose.

Future work should focus on extending the short-range proton treatment to the other investigated cell lines, further experimental validation, and application to more

realistic BNCT irradiation scenarios.

In conclusion, this thesis demonstrates the potential of BIANCA to provide cell-specific, energy-dependent radiobiological parameters for the complex mixed radiation field of BNCT. The extension and generation of radiobiological databases, together with the development of a short-range proton treatment, provide a basis for a more detailed description of radiation-induced biological effects. Their application within the extended Photon Isoeffective Dose model represents a methodological advance towards linking the physical characteristics of secondary particles to the predicted biological response in healthy and tumour tissues.

Appendix

Photon type	**CL** $Gy^{-1}cell^{-1}$	**f**
X 250 kVp	1.4	0.08
Co-60	1.1	0.08
6 MV	1.06	0.08

Table 1: parameters for V79 for the calculation of CL of the corresponding line of interest

Cell type	**Volume** μm^3
V79	678.24
HSF(AG15522)	628
HNSCC	678.24
U87	748.37504

Table 2: volume values for the corresponding line of interest

Position	**Depth (mm)**	**LET (keV/μm)**	α **(Gy^{-1})**	β **(Gy^{-2})**
P1	1.69	1.11 ± 0.03	0.14 ± 0.02	0.064 ± 0.009
P2	28.21	4.02 ± 0.16	0.17 ± 0.04	0.065 ± 0.009
P3	29.28	7.0 ± 0.9	0.22 ± 0.02	0.064 ± 0.0017
P4	29.76	11.9 ± 1.5	0.44 ± 0.06	0.045 ± 0.009
P5	30.24	18.0 ± 1.4	0.77 ± 0.08	0.008 ± 0.003
P6	30.72	22.6 ± 1.2	0.90 ± 0.13	0.010 ± 0.006

Table 3: depth, dose-averaged LET, and linear-quadratic cell survival parameters for U-87 cells, as reported by Chaudhary et al. [50].

E (keV)	Range (μm)	LET_0	LET_{track}	LET_{BIANCA}	CL_{track}	CL_{BIANCA}	f
1	0.0306	19.97	32.68	0.25	0.02925	0.000192	0.54
5	0.1298	36.89	38.52	1.25	0.03200	0.0010384	0.54
10	0.2265	50.01	44.15	2.50	0.03200	0.001812	0.54
20	0.3783	67.59	52.87	5.00	0.03200	0.0030264	0.54
30	0.5040	78.87	59.52	7.50	0.03200	0.004032	0.54
40	0.6171	86.23	64.82	10.00	0.03200	0.0049368	0.54
50	0.7234	90.81	69.12	12.50	0.03200	0.0057872	0.54
70	0.9270	94.47	75.51	17.50	0.03200	0.007416	0.54
100	1.2300	92.29	81.30	25.00	0.03200	0.00984	0.54
200	2.4000	71.81	83.33	50.00	0.03200	0.0192	0.54
300	3.9100	59.04	73.89	69.463	0.03200	0.031529	0.54
400	5.7700	49.33	66.78	49.33	0.03200	0.032000	0.54
500	7.9400	42.76	60.61	42.76	0.03200	0.032000	0.54
600	10.4200	37.99	55.45	37.99	0.03200	0.032000	0.54
700	13.1800	34.37	51.17	34.37	0.02974	0.0311	0.54
800	16.2100	31.53	47.53	31.53	0.02684	0.02803	0.54

Table 4: effective parameters used as input to BIANCA for fibroblast cells with $L_{cell} = 4\mu m$. The table reports the proton kinetic energy, range, initial *LET* (LET_0), track-averaged *LET(E/R)*, corrected BIANCA LET, track-level cluster lesion yield, geometrically rescaled BIANCA cluster lesion yield, and the LET-dependent f parameter. For short-range protons, CL_{track} and f were evaluated at $LET_{track} = E/R$. For traversing protons, they were evaluated at LET_0. Saturation was applied above the highest tabulated LET values.

Table 5: Radiobiological Parameters (α and β) for Reference Photons and Heavy Ions across Different LET Regimes

LET (keV/μm)	$\boldsymbol{\alpha}$ (Gy^{-1})	$\boldsymbol{\beta}$ (Gy^{-2})
Photon Reference		
Type: Co-60		
–	0.21	0.02
Protons ($Z = 1$)		
0.5	0.2100000000	0.02000000000
2.5	0.2134850173	0.01731014405
5.0	0.2534949856	0.02172123447
7.5	0.3356654697	0.01927739703
10.0	0.4166933658	0.01472649924
12.5	0.4157161310	0.02569258219
15.0	0.3794939168	0.04278774447
17.5	0.5393356048	0.02411692245
20.0	0.6765996605	0.01352172568
22.5	0.7166373093	0.01357952905
25.0	0.8257379648	0.009687987145
27.5	0.9886760564	0.006435060477
30.0	0.8962009387	0.01739929389
32.5	0.8004327264	0.005252844628
35.0	1.0311098490	0.001398112188
37.5	0.9200284278	0.02353177873
40.0	0.9458458475	0.01996154310
Helium and Lithium ($Z = 2, 3$)		
0.5	0.2100000000	0.02000000000
5.0	0.1812336584	0.03164981104
10.0	0.2450755036	0.03635906419
20.0	0.3890241117	0.05053389233
30.0	0.5647576440	0.05586053960
40.0	0.7695750217	0.05075936144
50.0	0.9511167426	0.05227487470
60.0	1.1110883310	0.05826777430
70.0	1.2672131990	0.04608127499

Table 5: Radiobiological Parameters (α and β) for Reference Photons and Heavy Ions across Different LET Regimes

LET (keV/μm)	$\boldsymbol{\alpha}$ (Gy^{-1})	$\boldsymbol{\beta}$ (Gy^{-2})
80.0	1.3831543030	0.04211545112
90.0	1.4881017860	0.03012668773
100.0	1.5735821270	0.01677139604
110.0	1.6100746040	0.01552236322
120.0	1.6260817960	0.02148392107
130.0	1.6377949640	0.01336215289
140.0	1.5805101170	0.01420546618
150.0	1.5415328800	0.00000000000
160.0	1.4707686010	0.00000000000
170.0	1.4170904580	0.00000000000
180.0	1.3560453190	0.00000000000
190.0	1.3026926040	0.00000000000
200.0	1.2546285010	0.00000000000
210.0	1.1987680400	0.00000000000
220.0	1.1568136440	0.00000000000
230.0	1.1202110470	0.00000000000
Carbon ($Z = 4$)		
0.5	0.2100000000	0.02000000000
5.0	0.1900905618	0.03771738788
10.0	0.2396741030	0.04268197853
20.0	0.3504439436	0.04624387122
30.0	0.4593365357	0.05104463707
40.0	0.5917741442	0.04794369576
50.0	0.6947524955	0.05706167573
60.0	0.8354867711	0.05153603415
70.0	0.9454812338	0.05216396967
80.0	1.0663106570	0.04584899799
90.0	1.1906754380	0.04395038090
100.0	1.2982353370	0.04441263471
110.0	1.3982014150	0.03527279023
120.0	1.4744903640	0.03095868961
130.0	1.5778816970	0.01458919479
140.0	1.6145779190	0.02845118122

Table 5: Radiobiological Parameters (α and β) for Reference Photons and Heavy Ions across Different LET Regimes

LET (keV/μm)	$\boldsymbol{\alpha}$ (Gy^{-1})	$\boldsymbol{\beta}$ (Gy^{-2})
150.0	1.7000435000	0.00000000000
175.0	1.7526367520	0.00000000000
200.0	1.6535203780	0.00000000000
225.0	1.5552600040	0.00000000000
250.0	1.4698844780	0.00000000000
275.0	1.3730817940	0.00000000000
300.0	1.2939045670	0.00000000000
325.0	1.2044986240	0.00000000000
350.0	1.1433536750	0.00000000000
375.0	1.0773632170	0.00000000000
400.0	1.0191305320	0.00000000000
425.0	0.9718003176	0.00000000000
450.0	0.9319637358	0.00000000000
475.0	0.8873495853	0.00000000000
500.0	0.8345465230	0.00000000000

Bibliography

[1] R. F. Barth, M. Graca H Vicente, O. K. Harling, W. S. Kiger III, K. J. Riley, P. J. Binns, F. M. Wagner, M. Suzuki, T. Aihara, I. Kato, and S. Kawabata. Current status of boron neutron capture therapy of high grade gliomas and recurrent head and neck cancer. *Radiation Oncology, 7:146*, 2012.

[2] F. Issa, J. A. Ioppolo, L. M. Rendina, J. Reedijk, and K. Poeppelmeier. Boron and gadolinium neutron capture therapy. *Elsevier Amsterdam*, 2013.

[3] R.F. Barth, J. A Coderre, M.G Vicente, and T.E Blue. Boron neutron capture therapy of cancer: current status and future prospects. *Clin Cancer Res*, 2005.

[4] M. Sibrian-Vazquez and M.G.H Vicente. Boron tumor-delivery for bnct: Recent developments and perspectives. in boron science: New technologies & applications. *CRC Press*, 2011.

[5] F. Hanif, K. Muzaffar, K. Perveen, S. Malhi, and S. Simjee. Glioblastoma multiforme: A review of its epidemiology and pathogenesis through clinical presentation and treatment. *Asian Pacific Journal of Cancer Prevention*, 2017.

[6] R.L. Moss. Critical review, with an optimistic outlook, on boron neutron capture therapy (bnct). *Applied Radiation and Isotopes*, 2014.

[7] T.D Malouff, D.S. Seneviratne, D.K. Ebner, W.C Stross, M.R Waddle, D.M. Trifiletti, and S. Krishnan. Boron neutron capture therapy: A review of clinical applications. *Frontiers in oncology*, 2021.

[8] S. Kawabata, M. Suzuki, K. Hirose, H. Tanaka, T. Kato, H. Narita, and S-I. Miyatake. Accelerator-based bnct for patients with recurrent glioblastoma: a multicenter phase ii study,. *Neuro-Oncology Advances*, 2021.

[9] S. Bortolussi, N. Protti, M. Ferrari, I. Postuma, S. Fatemi, M. Prata, F. Ballarini, M.P. Carante, R. Farias, S.J. González, M. Marrale, S. Gallo, A. Bartolotta, G. Iacoviello, D. Nigg, and S. Altieri. Neutron flux and gamma dose measurement in

the bnct irradiation facility at the triga reactor of the university of pavia. *Elsevier Amsterdam*, 2023.

[10] I. Postuma, S. González, M.S. Herrera, L. Provenzano, M. Ferrarini, V. Vercesi G. Battistoni, U. Anselmi Tamburini, Y. Hao Liu, and L. Kankaanranta. A novel approach to design and evaluate bnct neutron beams combining physical, radiobiological and dosimetric figures of merit. *Biology*, 2017.

[11] J.A. Coderre and G.M. Morris. The radiation biology of boron neutron capture therapy. *Radiation research*, 1999.

[12] ICRU. Report 46, photon, electron, proton and neutron interaction data for body tissues. *International Commission on Radiation Units and Measurements, Vol 32, Issue 1, Bethesda*, 1992.

[13] J. A. Coderre, M. S. Makar, P. L. Micca, M. M. Nawrocky, H. B. Liu, D. D. Joel, D. N. Slatkin, and H. I. Amols. Derivations of relative biological effectiveness for the high-let radiations produced during boron neutron capture irradiations of the 9l rat gliosarcoma in vitro and in vivo. *International Journal of Radiation Oncology Biology Physics*, 1993.

[14] T. Sato, S. Masunga, H. Kumada, and N. Hamada. Depth distributions of rbe-weighted dose and photon-isoeffective dose for boron neutron capture therapy. *Radiation protection dosimetry*, 2021.

[15] S. J. González and G. A. Santa Cruz. The photon-isoeffective dose in boron neutron capture therapy. *Radiation research*, 2021.

[16] A.M. Kellerer and H. H. Rossi. The theory of dual radiation action. *Curr Top Radiat Res Q*, 1972.

[17] H. H. Rossi and M. Zaider. Compound dual radiation action. *General aspects. Radiat.*, 1992.

[18] D.E Lea DE and D. G Catcheside. The mechanism of induction by radiation of chromosome aberrations in tradescandia. *J Genet*, 1942.

[19] D.E Lea. Action of radiation on living cells. *London: Cambridge University Press*, 1946.

[20] B. G Douglas and J. F Fowler. The effect of multiple small doses of x rays on skin reactions in the mouse and a basic interpretation. *Radiat Res*, 1976.

[21] T. E Schmid, G. Dollinger, W. Beisker, V. Hable, C. Greubel, S. Auer, A. Mittag, A. Tarnok, A. A. Friedl, M. Molls, and B. Röper. Differences in the kinetics of γ-h2ax fluorescence decay after exposure to low and high let radiation. *Int J Radiat Biol*, 2010.

[22] M. Zaider and H. H. Rossi. The synergistic effect of different radiations. *Radiat Res.*, 1980.

[23] A. M Dattoli Viegas, S. Ossio, J. Riback, L. M. Valeriano, G. Santa Cruz, A. Casali, M. P. Carante, F. Ballarini, S. Fatemi, I. Postuma, V. Vercesi, S. Bortolussi, and R. L. Ramos S. J. González. An extended photon isoeffective dose model accounting for the energy-dependent effectiveness of secondary charged particles in bnct. *Medical Physics*, 2026.

[24] F. Ballarini, S. Altieri, S. Bortolussi, M. Carante, E. Giroletti, and N. Protti. The bianca model/code of radiation-induced cell death: application to human cells exposed to different radiation types. *Radiat Environ Biophys.*, 2014.

[25] A. Ottolenghi, F. Ballarini, and M. Merzagora. Modelling radiation induced biological lesions: from initial energy depositions to chromosome aberrations. *Radiat. Environ. Biophys*, 1999.

[26] M.P. Carante, JT. Cajiao, and F. Ballarini F. The bianca model/code of radiation-induced cell death: Application to human cells exposed to different radiation types. *Radiat Meas.*, 2015.

[27] M.P. Carante, C. Aimè, J.J Tello Cajiao F, and Ballarini. Bianca, a biophysical model of cell survival and chromosome damage by protons, c-ions and he-ions at energies and doses used in hadrontherapy. *Phys. Med. Biol.*, 2018.

[28] F. Ballarini, S. Altieri AND0 S. Bortolussi, M. Carante, E. Giroletti, and N. Protti. A model of radiation-induced cell killing: insights into mechanisms and applications for hadron therapy. *Radiat. Res.*, 2013.

[29] M.P. Carante, S. Altieri, S. Bortolussi, I. Postuma, N. Protti, and F. Ballarini. Modelling radiation-induced cell death: role of different levels of dna damage clustering. *Radiat. Environ. Biophys.*, 2015.

[30] F. Ballarini and M.P. Carante. Chromosome aberrations and cell death by ionizing radiation: evolution of a biophysical model. *Radiat.Phys. Chem.*, 2016.

[31] M.P. Carante and F. Ballarini. Calculating variations in biological effectiveness for a 62 mev proton beam. *Frontiers Oncol*, 2016.

[32] M.P. Carante and F. Ballarini. Modelling cell death for cancer hadrontherapy. *AIMS Biophys.*, (2017).

[33] A. Chatterjee and H.J. Schaefer. Mittercrodosimetric structure of heavy ion tracks in tissue. *Radiat Environ Biophys 13*, 1976.

[34] M.P. Carante, G. Aricò, A. Ferrari, W. Kozlowska, A. Mairani, and F. Ballarini. First benchmarking of the bianca model for cell survival predictions in a clinical hadron therapy scenario. *Phys. Med. Biol. 64/21 215008*, 2019.

[35] M.P. Carante, G. Aricò, A. Ferrari, C.P. Karger, W. Kozlowska, A. Mairani, P. Sala, and F. Ballarini. In vivo validation of the bianca biophysical model: benchmarking against rat spinal cord rbe data. *Int. J. Mol. Sci. 21 3973*, 2020.

[36] M. Belli, F. Cera, R. Cherubini, M. Dalla Vecchia, A.M.I. Haque, F. Iazini, G. Moschini, O. Sapora, G. Simone, M.A. Tabocchini, and P. Tiveron. Rbe-let relationship for cell inactivation and mutation induced by low energy protons in v79 cells: further results at the lnl facility. *Int J Radiat Biol*, 1998.

[37] M. Folkard, K.M. Prise, B. Vojnovic, H.C. Newman, M.J. Roper, and B.D Michael. Inactivation of v79 cells by low-energy protons, deuterons and helium-3 ions. *Int J Radiat Biol*, 1996.

[38] Y. Furusawa, K. Fukutsu, M. Aoki, H. Itsukaichi, K. Eguchi-Kasai, H. Ohara, F. Yatagai, T. Kanai, and K. Ando K. Inactivation of aerobic and hypoxic cells from three different cell lines by accelerated 3he-, 12c- and 20ne-ion beams. *Radiat. Res.*, 2000.

[39] F. Rossi, G. Magni, F. Tatini, M. Banchelli, F. Cherchi, M. Rossi, E. Coppi, A.M. Pugliese, D. Rossi degl'Innocenti, D. Alfieri, F.S. Pavone, R. Pini, and P. Matteini. Photobiomodulation of human fibroblasts and keratinocytes with blue light: Implications in wound healing. *Biomedicines*, 2021.

[40] P. Boukamp, R.T. Petrussevska, D. Breitkreutz, J. Hornung, A. Markham, and N.E Fusenig. Normal keratinization in a spontaneously immortalized aneuploid human keratinocyte cell line. *Journal of Cell Biology*, 1988.

[41] S.S. Ningsih, S.W.A. Jusman, R. Syaidah, R. Nauli, and F. Fadilah. Efficient protocol for isolating human fibroblast from primary skin cell cultures: application to keloid, hypertrophic scar, and normal skin biopsies. *Biol Methods Protoc.*, 2024.

[42] J.A. Benanti and D.A. Galloway DA. Normal human fibroblasts are resistant to ras-induced senescence. *Mol Cell Biol.*, 2004.

[43] S. Chiblak, Z. Tang, D. Lemke, M. Knoll, I. Dokic, R. Warta, M. Moustafa, W. Mier, S. Brons, C. Rapp, S. Muschal, P. Seidel, M. Bendszus, S. Adeberg, O.D. Wiestler, U. Haberkorn, J. Debus, C. Herold-Mende, W. Wick, and A. Abdollahi. Carbon irradiation overcomes glioma radioresistance by eradicating stem cells and forming an antiangiogenic and immunopermissive niche. *JCI Insight*, 2015.

[44] M. Beuve, G. Alphonse, M. Maalouf, A. Colliaux, P. Battiston-Montagne, P. Jalade, E. Balanzat, A. Demeyer, M. Bajard, and C. Rodriguez-Lafrasse. Radiobiologic parameters and local effect model predictions for head-and-neck squamous cell carcinomas exposed to high linear energy transfer ions. *Int J Radiat Oncol Biol Phys*, 2008.

[45] B. Accotto. Tissue-specific radiobiological modeling for space radiation risk assessment. Master's thesis, Università di Pavia, 2026.

[46] W.S. Kozłowska, M.P. Carante, G. Aricò, A. Embriaco, A. Ferrari, G. Magro, A. Mairani, R. Ramos, P. Sala, D. Georg, and F. Ballarini. First application of the bianca biophysical model to carbon-ion patient cases. *Phys Med Biol.*, 2022.

[47] B. Marcaccio, M. Crepaldi, I. Postuma, E. Simeone, C. Guidi, S. Fatemi, R.L. Ramos, V. Vercesi, C. Ferrari, L. Cansolino, E. Delgrosso, R.D. Liberto, D. Dondi, D. Vadivel, Y.W. Chen, F.I Chou, J.J. Peir, C.J. Wu, H.Y. Tsai, J.C. Lee, A.M. Portu, A.M.D. Viegas, S.J. González, and S. Bortolussi. Towards an adequate description of the dose-response relationship in bnct of glioblastoma multiforme. *Med Phys.*, 2025.

[48] S. Chiblak, Z. Tang, B. Campos, Z. Gal, A. Unterberg, J. Debus, C. Herold-Mende, and A. Abdollahi. Radiosensitivity of patient-derived glioma stem cell 3-dimensional cultures to photon, proton, and carbon irradiation. *International Journal of Radiation Oncology*Biology*Physics*, 2016.

[49] S.E. Combs, J. Bohl, T. Elsässer, K.J. Weber, D. Schulz-Ertner, J. Debus, and W.K. Weyrather. Radiobiological evaluation and correlation with the local effect model (lem) of carbon ion radiation therapy and temozolomide in glioblastoma cell lines. *International Journal of Radiation Biology*, 2009.

[50] P. Chaudhary, T.I. Marshall, F.M. Perozziello, L. Manti, J.C. Frederick, F. Hanton, S.J. McMahon, J.N. Kavanagh, G.A.P. Cirrone, F. Romano, K.M. Prise, and G. Schettino. Relative biological effectiveness variation along monoenergetic and modulated bragg peaks of a 62-mev therapeutic proton beam: A preclinical assessment. *International Journal of Radiation Oncology*Biology*Physics*, 2014.

[51] S. Mathot. Lübeck, germany. In *The Trasco-Spes RFQ, in Proceedings of the LINAC*, 2004.

[52] T. Sato, Y. Iwamoto, and S. Hashimoto. Recent improvements of the particle and heavy ion transport code system - phits version 3.33. *J Nucl Sci Technol.*, 2024.

[53] M. J. Berger, J. S. Coursey, M. A. Zucker, J. Chang, S. M. Seltzer, and P. M. Bergstrom. Stopping-Power & Range Tables for Electrons, Protons, and Helium Ions. NIST Standard Reference Database 124, National Institute of Standards and Technology, Gaithersburg, MD, 2017. NISTIR 4999, Last Update: July 2017.

[54] S. Wang, Z. Zhang, L. Miao, and Y. Li. Boron neutron capture therapy: Current status and challenges. *Front Oncol.*, 2022.

List of Figures

1.1 Most abundant elements found in the human body in percentage of total body weight [12] 10

1.2 RBE-weighted dose (dashed line) and the photon-isoeffective doses calculated assuming independent action (solid gray line) or synergistic action (solid black line) as a function of the total absorbed dose [15]. . . 13

2.1 probability of end-joining of the chromosome fragments in terms of the distance between the free-ends d and a threshold value d_0, fixed as mean distance between two adjacent chromosome territories. If $d < d_0$ chromosomes can rejoin, with an un-rejoining probability. Otherwise, no rejoining occurs [27] 21

2.2 schematic representation of three nuclear reactions relevant to BNCT in healthy tissue (region A) and tumor tissue (region B). These reactions may occur in both regions, although their relative contributions depend on the local neutron energy spectrum, tissue composition, and boron concentration: (1) thermal neutron capture on nitrogen $^{14}\mathrm{N}(n,p)^{14}\mathrm{C}$, (2) neutron elastic scattering on hydrogen $^{1}\mathrm{H}(n,n)p$, and (3) thermal neutron capture on boron $^{10}\mathrm{B}(n,\alpha)^{7}\mathrm{Li}$. 25

2.3 schematic representation of the two proton transport regimes considered in the effective-track formalism. (a) Traversing proton, with a physical range $R \geq L_{\mathrm{cell}}$, crossing the cell nucleus along its characteristic traversal length L_{cell}. (b) Short-range proton, with $R < L_{\mathrm{cell}}$, stopping within the cell nucleus. 29

2.4 Graphical representation of the main components of the simulation, from left to right: irradiation source, cylindrical phantom and physical outcome [15]. 35

3.1 α (top) and β (bottom) coefficients as a function of LET for head and neck squamous cell carcinoma (HNSCC). Filled symbols represent the newly calculated values extending the database to the BNCT-relevant LET range. 38
3.2 α (top) and β (bottom) coefficients as a function of LET for immortalized human keratinocytes (HaCaT). Filled symbols represent the newly calculated values extending the database to the BNCT-relevant LET range. 39
3.3 comparison of the survival fraction between the different photon irradiations of the selected experimental datasets. 41
3.4 comparison between experimental U-87 cell survival data and BIANCA predictions for proton and carbon-ion irradiation. 43
3.5 α (top) and β (bottom) coefficients as a function of LET for U87 cells. 45
3.6 α (top) and β (bottom) coefficients as a function of LET for human skin fibroblasts (HSF). Filled symbols represent the newly calculated values extending the database to the BNCT-relevant LET range. 46
3.7 α coefficients as a function of the track-averaged LET for Human Skin Fibroblast (HSF) in the different regimes. 47
3.8 proton production as a function of kinetic energy at a superficial depth of 1.1 mm (region R_1). 49
3.9 dose imparted by secondary protons as a function of kinetic energy at 1.1 mm depth (region R_1). 50
3.10 relative contribution of individual dose components to the total absorbed dose at 1.1 mm depth in region R_1 (^{10}B concentration of 22.5 ppm). 51
3.11 comparison between the extended photon isoeffective dose (D_{IsoE1}) and the dose-component-based approximation (D_{IsoE2}) for HSF cells in region R_1 (1.1 mm depth), including their relative percentage difference as a function of total absorbed dose. 52
3.12 relative contribution of individual dose components to the total absorbed dose at 2.25 cm depth in region R_2 (^{10}B concentration of 52.5 ppm). 53
3.13 comparison between the extended photon isoeffective dose (D_{IsoE1}) and the dose-component-based approximation (D_{IsoE2}) for (a) U-87 and (b) HNSCC cells in region R_2 (2.25 cm depth), including their relative percentage difference as a function of total absorbed dose. In panel (b), the two curves almost completely overlap, making the blue curve difficult to distinguish. 54

List of Tables

1 parameters for V79 for the calculation of CL of the corresponding line of interest 59
2 volume values for the corresponding line of interest 59
3 depth, dose-averaged LET, and linear-quadratic cell survival parameters for U-87 cells, as reported by Chaudhary et al. [50]. 59
4 effective parameters used as input to BIANCA for fibroblast cells with $L_{cell} = 4\mu m$. The table reports the proton kinetic energy, range, initial *LET* (LET_0), track-averaged *LET(E/R)*, corrected BIANCA LET, track-level cluster lesion yield, geometrically rescaled BIANCA cluster lesion yield, and the LET-dependent f parameter. For short-range protons, CL_{track} and f were evaluated at $LET_{track} = E/R$. For traversing protons, they were evaluated at LET_0. Saturation was applied above the highest tabulated LET values. 60
5 Radiobiological Parameters (α and β) for Reference Photons and Heavy Ions across Different LET Regimes 61
5 Radiobiological Parameters (α and β) for Reference Photons and Heavy Ions across Different LET Regimes 62
5 Radiobiological Parameters (α and β) for Reference Photons and Heavy Ions across Different LET Regimes 63

Acknowledgments

I want to start by thanking my family: my father, my mother, and my brother, who have loved and supported me unconditionally. Thank you for all your effort, love, and affection; even from a distance, you have always been there for me. I love you all, and quite simply, none of this would have been possible without you.
To the working group, starting with my supervisor, Prof. Ramos; thank you for your guidance and patience, for always making time for my questions, and for all the effort you contributed. To my co-supervisors, Prof. Ballarini and Prof. Dattoli: thank you for your corrections, advice, and all the time you dedicated.
To everyone I met during this journey. To my fellow master's students, who became a little family to me here—we shared countless experiences over these past two years; you will always be a part of me, and I will never forget you, wherever I may go. To my flatmates, Beatriz and Anas: thank you for always listening and offering the best advice. A special thank you to Beatriz, for always knowing exactly when a glass of wine and a good conversation were needed.
And a special note of gratitude to Riccardo, my boyfriend: thank you so much for always being by my side, even during the most difficult times, for taking such good care of me, and for welcoming me with so much warmth—both you and your family.